

## DOCTORAL THESIS

### Active plasmonic nanostructures

Hosseini Alast, Fatemeh

*Date of Award:*  
2017

[Link to publication](#)

#### General rights

Copyright and intellectual property rights for the publications made accessible in HKBU Scholars are retained by the authors and/or other copyright owners. In addition to the restrictions prescribed by the Copyright Ordinance of Hong Kong, all users and readers must also observe the following terms of use:

- Users may download and print one copy of any publication from HKBU Scholars for the purpose of private study or research
- Users cannot further distribute the material or use it for any profit-making activity or commercial gain
- To share publications in HKBU Scholars with others, users are welcome to freely distribute the permanent URL assigned to the publication

**HONG KONG BAPTIST UNIVERSITY**

**Doctor of Philosophy**

**THESIS ACCEPTANCE**

DATE: April 7, 2017

STUDENT'S NAME: Fatemeh HOSSEINI ALAST

THESIS TITLE: Active Plasmonic Nanostructures

This is to certify that the above student's thesis has been examined by the following panel members and has received full approval for acceptance in partial fulfillment of the requirements for the degree of Doctor of Philosophy.

Chairman: Prof. Wong Ricky N S  
Chair Professor, Department of Biology, HKBU  
(Designated by Dean of Faculty of Science)

Internal Members: Prof. Van Hove M. A.  
Head, Department of Physics, HKBU

Prof. So Shu Kong  
Professor, Department of Physics, HKBU

External Members: Prof. Chan Che Ting  
Chair Professor  
Department of Physics  
The Hong Kong University of Science and Technology  
Kowloon

Prof. Tsai Din Ping  
Director and Professor  
Research Center for Applied Sciences, Academia Sinica  
Taiwan

Proxy: Dr. Huang Jeffery  
Associate Professor, Department of Physics, HKBU  
(as proxy for Prof. Tsai Din Ping)

In-attendance: Prof. Cheah Kok Wai  
Chair Professor, Department of Physics, HKBU

Issued by Graduate School, HKBU

# **Active Plasmonic Nanostructures**

**Fatemeh HOSSEINI ALAST**

**A thesis submitted in partial fulfillment of the requirements**

**for the degree of**

**Doctor of Philosophy**

**Principal Supervisor: Prof. CHEAH Kok Wai**

**Hong Kong Baptist University**

**April 2017**

## DECLARATION

I hereby declare that this thesis represents my own work which has been done after registration for the degree of PhD at Hong Kong Baptist University, and has not been previously included in a thesis or dissertation submitted to this or any other institution for a degree, diploma or other qualifications.

I have read the University's current research ethics guidelines, and accept responsibility for the conduct of the procedures in accordance with the University's Committee on the Use of Human & Animal Subjects in Teaching and Research (HASC). I have attempted to identify all the risks related to this research that may arise in conducting this research, obtained the relevant ethical and/or safety approval (where applicable), and acknowledged my obligations and the rights of the participants.

Signature: *Fatemeh Alorfi*

Date: April 2017

**Abstract:**

In principle, the surface plasmon polaritons, at the planar metal/dielectric interface, cannot be excited by incident light. However momentum transfer from incident light to Surface Plasmon Polaritons (SPPs) inside the light line can be achieved by adding a periodic structure at the interface. The lattice wave vector can compensate the difference between incident light and surface wave momentum and satisfy momentum matching requirement. Two methods are commonly used to achieve this goal: first, using prism and second, surface engineering using different array apertures at the metal/dielectric interfaces.

In this thesis, the ruled grating pattern at the metal/dielectric interface using conventional photolithography technique was fabricated. The dimension of ruled grating pattern is proportional to expanding/collimating system in the interference set-up. In fact, a large area grating can be utilized for many optoelectronic applications with greater efficiency. In this work, large area grating pattern,  $10 \times 10 \text{ mm}^2$ , on top of the microcavity structure was integrated that permitting cavity mode-SPP coupling. Hence, Rabi-like splitting was observed from the hybrid plasmonic microcavity. The splitting was created from the coupling of cavity mode with the surface plasmon polariton mode; anti-crossing was observed alongside the modal conversional channel on the reflection light measurement.

In following, it was experimentally explored the effect of using organic fluorescent molecules inside the hybrid plasmonic microcavity. Accordingly we integrated large area ruled metal grating onto photonic microcavity and assessed the cavity mode-SPP coupling with reflectivity measurement. We got much more grounded modal coupling in presence of florescent molecules within photonic cavity. The anti-crossing was detected with enormous Rabi-like splitting energy at 280 meV in the strong coupling regime. Besides we compared the coupling strength of plasmonic microcavities with various cavity lengths to explore the absorption impact.

## Acknowledgement

بِسْمِ اللَّهِ الرَّحْمَنِ الرَّحِيمِ

In the name of God, the compassionate the merciful

First and above all, I praise **Allah**, the almighty for providing me this opportunity and granting me the capability to proceed successfully. I express my cordial thanks to **Imam Mahdi** who I always feel his attendance and pray in all moments of life, may **Allah** hasten his blissful return with **Jesus**.

I appreciate my supervisor **Prof. Cheah** to provide me the opportunity of worthy academic experience and express my sincere gratitude to him for his generous support, insightful comments and warm encouragements during my PhD study.

Thank you to those who helped the project as staff and graduate students; **Dr. Hoi Lam, Dr. Amy Ching, Dr. Zhang Lu, Mr. Stanley Tse, Mr. Benson Leung** and other group members of **Institute of Advance Materials**.

I would like to express my sincere thanks to my love, my best friend and better half, **Saeed Rezaei**, who never has left me alone and stood by my side and invariably put up with the hardship of my study condition, long distance and longtime of separation. Surely I could not have completed my degree without his compassionately supports and understandings; therefore, I can just say thanks for everything.

I would like to warmly thank and appreciate my dear parents, **Seyed Ahmad** and **Hoda**, who devoted all their life for us and do all their best. I acknowledge their great patience and praiseworthy teaching of true life style which the education is worthless without the pursuit of a moral and religious life. I warmly appreciate my dear sister and friend, **Faezeh**, for her spiritual support and her help of text editing during my study. And also many thanks to my brother, **Ali**, for his support and creating a happy environment in our family.

## Table of Contents

Abstract:.....	i
Acknowledgement .....	iii
Table of Contents .....	v
List of Figures .....	viii
List of Tables.....	xii
Chapter 1 Introduction .....	1
1.1 Surface Plasmon Polariton.....	2
1.2 Extraordinary Transmission.....	3
1.3 Plasmonic Microcavities and Rabi-like Splitting .....	4
1.4 Passive and Active Plasmonic Microcavities .....	6
1.5 Photolithography Technique.....	7
1.6 The scope of research .....	8
Chapter 2 Theory.....	11
2.1 Plasmonic Nanostructures .....	11
2.1.1 TEM modes on metal/dielectric interface.....	12
2.1.2 The Effective parameters on coupling strength of plasmonic nanostructures .....	20
2.1.2.1 Material types in Plasmonic Nanostructure .....	20
2.1.2.2 Size and Shape of Plasmonic Nanostructures .....	22
2.1.2.3 The Lattice Finite-Size .....	24
2.1.3 Resonance Field Coupling Mechanism .....	24

2.1.3.1 The Near-Field Coupling .....	25
2.1.3.1.1 Electric and Magnetic Dipoles .....	26
2.1.3.1.2 The Mirror Effect .....	27
2.1.3.2 The Far-Field Coupling .....	27
2.1.3.2.1 The Phase Retardation Model .....	27
2.1.3.3 The Quantum Description of Coupling of Single Emitters with Resonance Filed .....	30
2.1.3.4 The Classical Description of Coupling of Surface Plasmon Polariton and Resonance Field .....	34
2.1.3.5 The SPP-Emitter Strong Coupling with Damping Rates.....	38
2.1.3.6 The Strong Modal Coupling from Plasmonic Microcavities .....	39
2.2 Photolithography Technique.....	45
2.2.1 Optical Lithography .....	46
2.2.2 Photoresist.....	47
2.2.3 Laser Interference.....	49
Chapter 3 Fabrication Technique Fabrication Technique.....	53
3.1 Photolithography .....	53
3.1.1 Substrate Preparation.....	54
3.1.2 Solution Preparation .....	54
3.1.3 Photoresist Film Coating .....	56
3.1.4 Lithography.....	57
3.1.4.1 Optical Mask .....	58
3.1.4.2 Optimization of Light Exposure Dose and Developing Time .....	60
3.2 Metallic Thin Film Deposition by Thermal Evaporation.....	61
3.3 Grating Characterization .....	62

3.3.1 Scanning Electron Microscopy for Surface Analysis.....	62
3.3.2 Ellipsometric Measurement of SPP Mode.....	65
3.3.3 SPP Mode Calculation.....	67
3.4 Liftoff Technique .....	68
Chapter 4 Plasmonic Microcavities.....	70
4.1 Passive Plasmonic Microcavity .....	70
4.1.1 Introduction of Exerted Materials .....	71
4.1.2 Structure of Fabricated Plasmonic Cavity .....	72
4.1.3 Reflection Measurement Analysis for Different Cavity Thicknesses.....	73
4.1.3.1 Passive Plasmonic Microcavity with Photoresist Medium.....	73
4.1.3.2 Passive Plasmonic Microcavity with PMMA Medium .....	76
4.2 Active Plasmonic Microcavity.....	81
4. 2. 1 Active Plasmonic Microcavity Structure.....	83
4. 2. 2 The Material Characterization of Intermediate Dielectric Layer of Photonic Cavity .....	84
4. 2. 3 Results and Discussion .....	86
Chapter 5 Conclusion and Future Work .....	91
References .....	94
Curriculum Vitae .....	106

## List of Figures

Figure 1.1 The electric field distribution of SPPs at the metal surface [2].	3
Figure 1.2 Zero order transmission spectrum of square array with hole diameter=150nm and pitch size=0.9 $\mu\text{m}$ through silver film with thickness=200nm, the EOT occurs at $\lambda=1,370$ nm [4].	4
Figure 1.3 Splitting of normal mode of coupled atom-cavity system regarding to enhancement of coupling strength [6].	5
Figure 1.4 (a) Excitation of localized and surface plasmons of metal nanowires, (b) coupling of two distinct plasmon modes with cavity mode, the dispersion relation of photonic cavity and plasmon modes are intersected by tuning cavity length [7].	7
Figure 1.5 SEM images of large area nanohole array fabricated with photolithography (a) pattern on photoresist film, (b) gold periodic nanohole array film after liftoff, height of pillar=600 nm, hole diameter=240 nm, pitch size=700 nm [8].	8
Figure 2.1 one-dimensional metal layer.	14
Figure 2.2 Using prism to couple incident light with SPP; (a) Otto (b) Kretschmann configuration [39].	19
Figure 2.3 Momentum matching condition on the corrugated interface [36].	20
Figure 2.4 the effect of different metals on the EOT through plasmonic nanostructure, (a) experimental [40], (b) theoretical [41] results.	22
Figure 2.5 the transmission spectra of rectangular aperture with varying period, for the polarization (a) perpendicular to the short edge (b) perpendicular to the long edge.	23
Figure 2.6 the dipole electric field diagram of coupled nanoparticles; (a) parallel (b) perpendicular to the incident electric field [63].	25

Figure 2.7 the symmetric and antisymmetric mode of the energy level hybridization of coupled plasmonic nanoparticles [63].	26
Figure 2.8 the coherent and incoherent interaction of single emitter with electric field of resonance structure [64].	30
Figure 2.9 Time evolution of interaction of the emitter and resonance structure under different coupling conditions [64].	33
Figure 2.10 the TE and TM (a,b) experimental and (c,d) simulation results of Rabi-like splitting for the plasmonic microcavity. The 2D periodic rectangular aperture array with 320 nm period was integrated onto the Fabry-Perot cavity.	45
Figure 2.11 The etched pattern fabricated with two type of photoresist; left: positive, Right: negative.	47
Figure 2.12 The schematic of linear and nonlinear photoresist performance.	48
Figure 2.13 The schematic of Michelson interferometer.	51
Figure 3.1 The schematic diagram of photolithography process.	57
Figure 3.2 The absorption spectrum of AP-R 5350 [85].	59
Figure 3.3 The interferometer setup.	59
Figure 3.4 Low quality grating patterns due to (a) over-exposure time and (b) overdeveloping time.	63
Figure 3.5 Low quality grating patterns due to insufficient time of light exposure and developing.	63
Figure 3.6 Low quality grating patterns caused by (a) environmental vibrations and (b) misalignment of interferometer setup.	63
Figure 3.7 Fabricated gratings with different pitch sizes, ( $\Lambda$ ), by photolithography, (a) $\Lambda=354$ nm, (b) $\Lambda=366$ nm, (c) $\Lambda=375$ nm, (d) $\Lambda=410$ nm, (e) $\Lambda=574$ nm.	64
Figure 3.8 Schematic diagram of ellipsometer setup [86].	65
Figure 3.9 Measurement of (a) amplitude and (b) phase change of first mode of SPP at different incident angles.	67

Figure 3.10 The calculation of the first mode of SPP excitation at varied incident angles.....	68
Figure 3.11 Lift-off technique diagram. ....	69
Figure 3.12 The flexible fabricated grating on soft substrate. ....	69
Figure 4.1 Optical properties of the exerted PMMA (polymethyl methacrylate) as dielectric medium of photonic cavity [95].....	72
Figure 4.2 The structure of fabricated plasmonic microcavity. ....	73
Figure 4.3 (a) cavity length is 200 nm and grating pitch size is 370 nm, (b) cavity length is 190 nm and grating pitch size is 370 nm, (c) cavity length is 170 nm and grating pitch size is 370 nm. ....	74
Figure 4.4 the reflectivity measurement of TM mode of three different regions of fabricated plasmonic microcavities for angles from 54 to 56 degrees. ....	75
Figure 4.5 The measured reflectivity of TM mode for the plasmonic microcavities with the silver grating period 390 nm and varying cavity length; (a) 1 $\mu$ m, (b) 1.2 $\mu$ m, (c) 500 nm.....	77
Figure 4.6 Rabi-like splitting at 49 degree (a), the measurement of TM mode coupling of SPPs and cavity modes with anti-crossing at 49 degree and conversional channel from 53 to 57 degree (b).....	78
Figure 4.7 Calculation of (a) SPP modes and (b) cavity modes for angles from 40 to 70 degree. ....	80
Figure 4.8 The TE mode reflection from designated cavity structure; (a) experimental and (b) calculation result.....	80
Figure 4.9 The low quality plasmonic microcavity because of the penetration of developing solution. ....	81
Figure 4.10 The hybrid plasmonic microcavity configuration and the SEM image of grating surface quality. ....	84
Figure 4.11 Molecular structure of Rubrene (116).....	85
Figure 4.12 The PL emission spectrum of Rubrene. ....	85
Figure 4.13 . The Rabi-like splitting of strong modal coupling (a) the plasmonic microcavity with 30nm Rubrene layer at 50 degree, (b) the	

plasmonic microcavity with 50nm Rubrene layer at 50 degree, (c) there is no coupling upon the plasmonic microcavity with 80 nm Rubrene layer. ....88  
Figure 4.14 The PL emission spectra from (a) the plasmonic and photonic microcavity, (b) Rubrene thin film coated on PMMA layer.....89

## **List of Tables**

Table 3.1 The photoresist, AP-R 5350, properties [83].	55
Table 3.2 Measured thickness of different spin-coated photoresist films.	55
Table 3.3 Optimized light exposure and developing time for two different photoresist film thicknesses on glass.	61
Table 3.4 Optimized light exposure and developing time for two different photoresist film thicknesses on silver substrate.	61

## **Chapter 1 Introduction**

Metals have been pointed out to be beneficial in light-matter interactions. Free electrons of vacancy layer among positive ion cores are responsible of distinct metal characteristics in which produce bulk plasma. Free charges oscillate in applied electromagnetic field. The quantum of oscillation is known as plasmon in bulk metal. The plasma frequency usually varies between 5 – 15 eV in the ultraviolet regime depending on metal type [1]. The oscillation of free charges at the metal surface generates surface electromagnetic waves that show novel optical properties with light interaction in symmetric or asymmetric environment.

In present work, we focused on surface plasmon behavior at the dielectric intersection. Surface plasmons can be excited on the corrugated metal surface so we used photolithography technique to fabricate large area metal ruled grating. The advantages of this technique are simple, cost-effective, which makes it possible for mass production of large area plasmonic structure. To investigate the reflection light behavior in hybrid plasmonic microcavities, the fabricated grating were integrated with passive and active microcavities respectively.

In this chapter, brief explanations of several essential concepts related to plasmonic properties and fabrication technique will be presented. Firstly, an introduction on surface plasmon and surface plasmon polariton is given in section 1.1, and then extraordinary transmission through plasmonic structure is explained in section 1.2. In section 1.3 and 1.4 plasmonic microcavities and Rabi-like splitting and passive and active plasmonic microcavities are discussed respectively. The photolithography technique is introduced in section 1.5 and the scope of research in section 1.6.

## **1.1 Surface Plasmon Polariton**

Free charges form non-propagating oscillations at the metal surface and the surface oscillations are confined on the metal surface due to their dispersion relation, resulting in evanescent wave decaying from both sides of the interface. These quasi-static electromagnetic modes called surface plasmon. The interaction of surface plasmon with incident light creates complex electron-photon oscillation modes at certain defined conditions, and these surface modes are known as surface plasmon polariton (SPP). The surface electromagnetic waves are evanescently confined perpendicular to metal surface due to the negative real part of dielectric function of metal ( $\text{Re}[\epsilon_M] < 0$ ) in the frequency regime below the plasma frequency of metal ( $\omega_P$ ) [1]. The electric field distribution is shown in the figure (1.1).

The confined SPPs field oscillates with an enhancement of the electric field strength near metal surface in which can be used for variety applications.

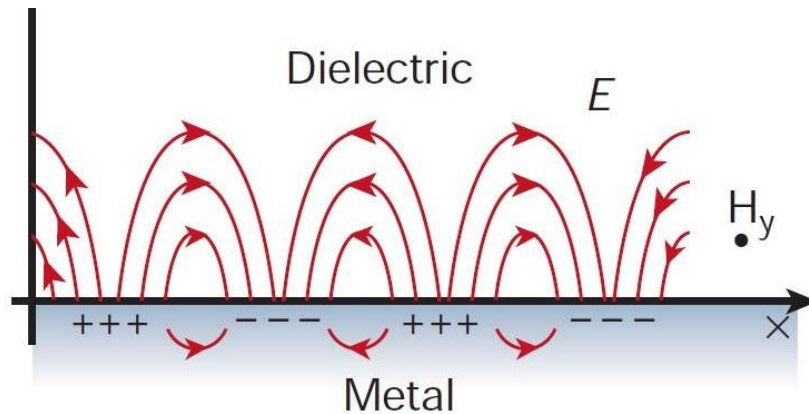


Figure 1.1 The electric field distribution of SPPs at the metal surface [2].

## 1.2 Extraordinary Transmission

Surface plasmon polaritons cannot be directly excited by incident plane wave regarding to outside line cone of the SPP dispersion relation. The phase matching condition at the metal/dielectric interface would be satisfied by surface engineering. Surface periodically modulation serves to compensate incident light wave vector in the dielectric environment with adding lattice wavevector in the momentum matching condition. Investigation has shown that there is extraordinary transmission (EOT) through array of apertures rather than the flat transparent metal film or milled individual aperture on metal surface film in which the efficiency exceeds unity (normalized to the total area of the holes) [3]. EOT of periodic structure means that it transmits

more light than a large area structure with the same area of all periodic subwavelength holes. Researchers believe that EOT occurs at the plasmonic metal/dielectric interface due to SPPs excitation and SPPs play significant role to transmit light through thin modulated metal film.

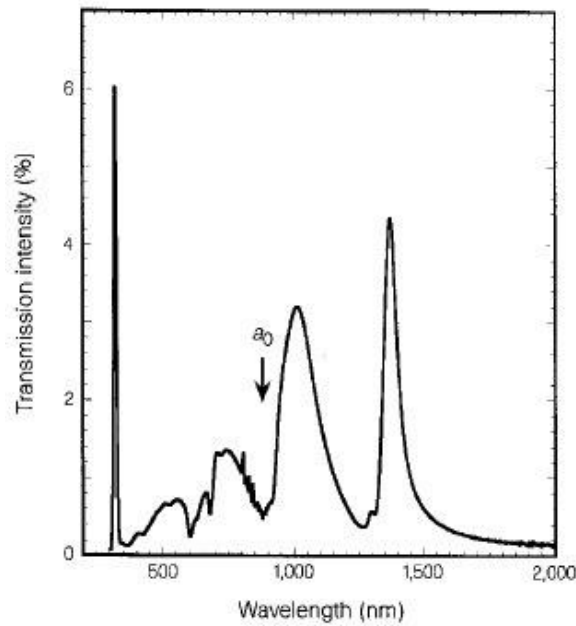


Figure 1.2 Zero order transmission spectrum of square array with hole diameter=150nm and pitch size=0.9  $\mu\text{m}$  through silver film with thickness=200nm, the EOT occurs at  $\lambda=1,370$  nm [4].

### 1.3 Plasmonic Microcavities and Rabi-like Splitting

Recently plasmonic nanostructure integrated with photonic devices can provide manipulated optical properties for various applications. The outstanding integrated plasmonic structure is hybrid plasmonic microcavities. Plasmonic periodic aperture can be fabricated on top or inlaid of photonic

cavity to support SPP-cavity mode coupling. The SPP-cavity mode coupling exhibits Rabi-like splitting in analogy to quantum electrodynamic phenomenon of Rabi-splitting in the interaction of a single emitter with resonant structures. Rabi-like splitting of plasmonic microcavities serves to improve performance of various optoelectronic devices by controlling and tailoring the energy distribution (e.g. polariton lasers) [5]. Rabi-like splitting can be theoretically investigated in classical regime with simple dipole approximation. Therefore, plasmonic microcavity provides novel optical characteristics for novel optoelectronic devices and it can be practically employed in different photonic devices for instance polaritons lasers, biosensors, metamaterial, organic/photonic-plasmonic systems.

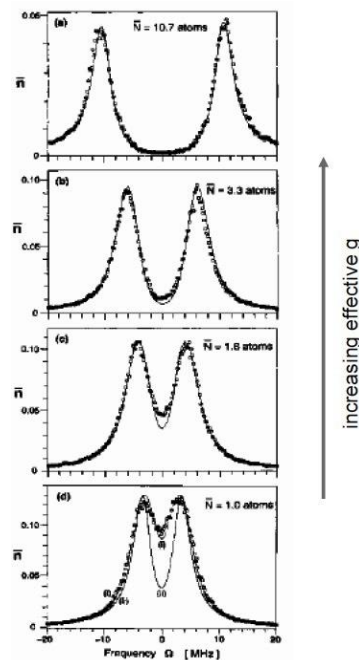


Figure 1.3 Splitting of normal mode of coupled atom-cavity system regarding to enhancement of coupling strength [6].

#### **1.4 Passive and Active Plasmonic Microcavities**

To fabricate hybrid plasmonic microcavity, Fabry-Perot cavity is usually designed as photonic cavity integrated with plasmonic nanostructures. Fabry-Perot cavity involves two parallel back and forward mirrors and also dielectric intermediate spacer such that the dielectric thickness can be tuned to achieve specific cavity modes in designated spectrum ranges. The cavity is filled by passive or active dielectric material. The passive dielectric intermediate layer only controls the spatial position of cavity mode in the optical spectrum by varying the dielectric thickness. While the active dielectric material can generate different optical effects, for example, nonlinear phenomena besides controlling cavity modes which are needed in some optoelectronic devices. Therefore via fabricating passive or active plasmonic microcavities regarding to selected intermediate material of photonic cavity, interesting physical light-matter interaction and coupling at the interface of cavity and plasmonic nanostructures can be explored.

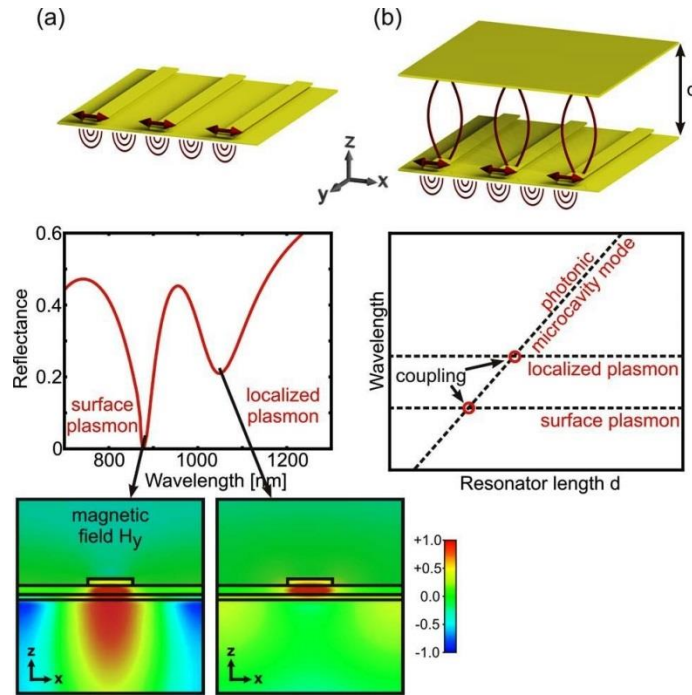


Figure 1.4 (a) Excitation of localized and surface plasmons of metal nanowires, (b) coupling of two distinct plasmon modes with cavity mode, the dispersion relation of photonic cavity and plasmon modes are intersected by tuning cavity length [7].

## 1.5 Photolithography Technique

To generate desired nano- or micro- structure on optoelectronic devices, there are different lithography techniques in which each one of them has its own pros and cons. Photolithography is a simple cost-effective technique to fabricate large area nanostructure pattern for various applications in industrial mass production. This technique requires a mask with designed pattern for specific application and also several lithography steps to transfer the pattern on photosensitive film. The made pattern on photosensitive film can be reproduced by molding techniques or transferring to soft substrate with lift-off techniques for subsequent application. The mask can be either made by laser

light as optical mask or designed as a printed mask under proper lamp projection. The wavelength of laser beam or emission spectrum of lamp source depends on the absorption spectrum of photosensitive material. So a wide range of subwavelength periodic structures can be produced using photolithography technique.

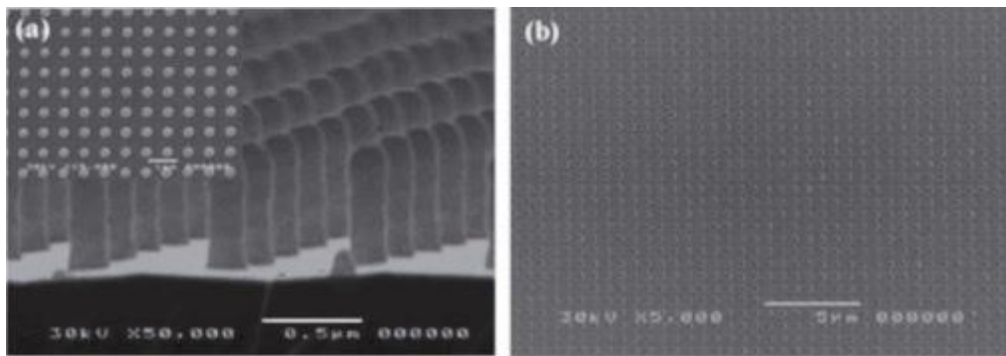


Figure 1.5 SEM images of large area nanohole array fabricated with photolithography (a) pattern on photoresist film, (b) gold periodic nanohole array film after liftoff, height of pillar=600 nm, hole diameter=240 nm, pitch size=700 nm [8].

## 1.6 The scope of research

Most challenging issue in the photonics research groups is resulting from wide range of photonics devices or molecular sensing and spectroscopy applications. The light transmission in metal/dielectric interface was investigated inserting the grating into the planar interface. Planar metal/dielectric cannot efficiently transmit the light because of low coupling between incident light and resonant surface modes regarding to momentum phase matching at the interface. The wave vector induced by periodic structure can compensate the difference between incident light and surface wave

momentum and satisfying the momentum matching requirement. Two common methods were used to achieve this goal: using prism and surface engineering using different array apertures at the metal/dielectric interface. In this study it was aimed to obtain optimal transmission efficiency using the subwavelength array apertures at the interface.

The grating pattern at the interface was fabricated using photolithography technique with the aid of optical interferometer and selected photosensitive material. It was then transferred to different substrates including flexible substrates by lift-off technique. The experiment was also implemented with different metal/dielectric structures and grating pitches.

In this thesis, metal ruled grating was integrated with Fabry-Perot cavity to produce hybrid plasmonic microcavity. Plasmonic nanostructure exhibits SPPs modes at the surface which coupled with cavity mode in reflected light. The SPP-cavity mode coupling resulted in an anti-crossing along Rabi-like splitting at common wavelength and specific angle of incident light. Here we took advantage of the hybrid plasmonic microcavity to observe SPP-cavity coupling and Rabi-like splitting of reflected light arisen from plasmonic microcavity surface.

Photonic Fabry-Perot cavity can be integrated with passive or active dielectric medium, which makes it possible investigate SPP-cavity mode coupling via passive and active plasmonic microcavity regarding to the optical behavior of dielectric material. In this work both passive and active plasmonic

microcavities were fabricated and their properties were measured compare with each other. The fabricated plasmonic microcavities could employ for various application to manipulate the optical properties and also tailor the energy distribution of different modes.

## Chapter 2 Theory

### 2.1 Plasmonic Nanostructures

The physical investigation of surface plasmons played a significant role to the understanding of many fundamental properties of solids in condensed matter and surface physics. Regarding energy loss investigation through thin metal film under fast electron beam, Ritchie found a new lowered loss at the film boundaries due to the excitation of surface collective oscillations, (1956) [9]. In 1959, Powell and Swan have shown the existence of these surface oscillations [10] and Stern and Ferrell defined the quanta of oscillations as the surface plasmon [11]. In fact, surface plasmons were employed in wide variety of applications; electrochemistry [12], wetting [13], biosensing [14-16], scanning tunneling microscopy, surface plasmon microscopy [17-18], surface plasmon resonance technology [19-25], extraordinary transmission through subwavelength array of apertures [26-27], nanoscale optoelectronic devices such as plasmonic microcavities and optical circuits [28-31], waveguides [32-33], modulators [34], switches [35] and so on.

Maxwell's equations can describe the metal behavior inside the electromagnetic field in classical model and results are reliable for metallic nanostructures due to high density of free charges in very small volume in comparison with thermal excitations of energy  $k_B T$  at room temperature,  $k_B$  is

Boltzmann constant and  $T$  is temperature. Metals exhibit different behavior in various frequency regimes. Metals are in general highly reflective in visible frequencies and behave as perfect conductor in low-frequency regime. Ultimately metals almost possess dielectric characters at ultraviolet frequency i. e. the electromagnetic field can propagate inside the metal regarding to its electronic band structure, for example alkali metals demonstrate transparent in ultraviolet regime meanwhile noble metals show strong absorption in this regime. Therefore the metal dispersion relation can be described with frequency-dependent dielectric function  $\epsilon(\omega)$  and determine the optical response of metal at different interfaces and frequency regimes [36].

### 2.1.1 TEM modes on metal/dielectric interface

The optical response at the metal/dielectric interface can be investigated by Maxwell's equations for resolving the components of EM fields of each layer of structure. The general Maxwell's equations are as follow:

$$\nabla \cdot \mathbf{D} = \rho_{\text{ext}} \quad 2-1$$

$$\nabla \cdot \mathbf{B} = 0 \quad 2-2$$

$$\nabla \times \mathbf{E} = -\frac{\partial \mathbf{B}}{\partial t} \quad 2-3$$

$$\nabla \times \mathbf{H} = \mathbf{J}_{\text{ext}} + \frac{\partial \mathbf{D}}{\partial t} \quad 2-4$$

Then curl equation is defined at the flat metal/dielectric interface:

$$\nabla \times \nabla \times \mathbf{E} = -\mu_0 \frac{\partial^2 \mathbf{D}}{\partial t^2} \quad 2-5$$

$$\nabla \times \nabla \times \mathbf{E} = \nabla(\nabla \cdot \mathbf{E}) - \nabla^2 \mathbf{E} \quad 2-6$$

$$\nabla \cdot (\epsilon \mathbf{E}) \equiv \mathbf{E} \cdot \nabla \epsilon + \epsilon \nabla \cdot \mathbf{E} \quad 2-7$$

In the absence of external electric field, it gets:

$$\nabla \cdot \mathbf{D} = 0 \quad 2-8$$

$$\nabla \left( -\frac{1}{\epsilon} \mathbf{E} \cdot \nabla \epsilon \right) - \nabla^2 \mathbf{E} = -\mu_0 \epsilon_0 \epsilon \frac{\partial^2 \mathbf{E}}{\partial t^2} \quad 2-9$$

By considering  $\epsilon$  as a constant Eq. (2-9) becomes:

$$\nabla^2 \mathbf{E} - \frac{\epsilon}{c^2} \frac{\partial^2 \mathbf{E}}{\partial t^2} = 0 \quad 2-10$$

The wave equation can be solved independently in different regions with constant ( $\epsilon$ ) and then the results can be matched at the interfaces with appropriate boundary conditions describing the physical phenomena in the defined structure [36].

The  $\mathbf{E}(\mathbf{r}, t)$  is a propagating wave, Eq. (2-11), and inserts into the Eq. (2.10):

$$\mathbf{E}(\mathbf{r}, t) = \mathbf{E}(\mathbf{r})e^{-i\omega t} \quad 2-11$$

$$\nabla^2 \mathbf{E} + k_0^2 \epsilon \mathbf{E} = 0 \quad 2-12$$

where  $k_0 = \omega/c$  is wave vector of the propagating wave in vacuum.

Finally, Eq. (2-12) is applied to the defined structure as shown in the figure (2.1) for describing one-dimensional problem. In figure (2.1), the wave propagates in x-direction and  $\epsilon$  varies in z-direction,  $\epsilon = \epsilon(z)$ , so the electric field propagates at the interface,  $Z=0$ , as below:

$$\mathbf{E}(x, y, z) = \mathbf{E}(z) e^{i\beta x} \quad 2-13$$

where  $\beta = k_x$  called the complex propagating constant corresponds to the wave vector component in the direction of propagation.

The wave equation can be obtained by applying Eq. (2-13) in the Eq. (2-12):

$$\frac{\partial^2 \mathbf{E}(z)}{\partial z^2} + (k_0^2 \epsilon - \beta^2) \mathbf{E} = 0 \quad 2-14$$

Similar equation can be obtained for the magnetic field, H, at the interface.



Figure 2.1 one-dimensional metal layer.

The explicit expressions for different components of E and H can be achieved by using Maxwell curl Eq. (2-3) and Eq. (2-4) to designate the spatial field distribution and the dispersion relation at the metal/dielectric interface.

By taking that the wave is propagating in sinusoidal form  $\left(\frac{\partial}{\partial t} = -i\omega\right)$  in x-direction  $\left(\frac{\partial}{\partial x} = i\beta\right)$  and homogeneity along y-direction, the following set of coupled equations get,

$$\frac{\partial E_z}{\partial z} = -i\omega\mu_0 H_x \quad 2-15$$

$$\frac{\partial E_x}{\partial z} - i\beta E_z = i\omega\mu_0 H_y \quad 2-16$$

$$i\beta E_y = i\omega\mu_0 H_z \quad 2-17$$

$$\frac{\partial H_y}{\partial z} = i\omega\varepsilon_0 \varepsilon E_x \quad 2-18$$

$$\frac{\partial H_x}{\partial z} - i\beta H_z = -i\omega\varepsilon_0 \varepsilon E_y \quad 2-19$$

$$i\beta H_y = -i\omega\varepsilon_0 \varepsilon E_z \quad 2-20$$

Considering two modes of polarization separately, first the transverse magnetic mode (TM or p) in which only  $E_x$ ,  $E_z$  and  $H_y$  are nonzero,

$$E_x = -i \frac{1}{\omega\varepsilon_0 \varepsilon} \frac{\partial H_y}{\partial z} \quad 2-21$$

$$\mathbf{E}_z = -\frac{\beta}{\omega \varepsilon_0 \varepsilon} \mathbf{H}_y \quad 2-22$$

Then the TM mode wave equation from the Eq. (2-14) obtains,

$$\frac{\partial^2 \mathbf{H}_y}{\partial z^2} + (k_0^2 \varepsilon - \beta^2) \mathbf{H}_y = 0 \quad 2-23$$

On the other hand, the TE mode has nonzero component fields of  $H_x$ ,  $H_z$  and  $E_y$ :

$$\mathbf{H}_x = i \frac{1}{\omega \mu_0} \frac{\partial \mathbf{E}_y}{\partial z} \quad 2-24$$

$$\mathbf{H}_z = \frac{\beta}{\omega \mu_0} \mathbf{E}_y \quad 2-25$$

The TE mode wave equation from the Eq. (2-14) gets:

$$\frac{\partial^2 \mathbf{E}_y}{\partial z^2} + (k_0^2 \varepsilon - \beta^2) \mathbf{E}_y = 0 \quad 2-26$$

These equations serve to investigate the light behavior at the dielectric and perforated metal interfaces.

The SPPs exist in a flat interface of non-absorbing dielectric with positive real dielectric constant ( $\varepsilon_2$ ) and conductor with negative real part of dielectric function [ $\text{Re}(\varepsilon_1) < 0$ ]. This condition can be satisfied for metal at frequencies below the bulk plasma frequency  $\omega_p$ .

TM solutions are obtained at the interface,

for  $z > 0$ ,

$$H_y(z) = A_2 e^{i\beta x} e^{-k_2 z} \quad 2-27$$

$$E_x(z) = iA_2 \frac{1}{\omega \varepsilon_0 \varepsilon_2} k_2 e^{i\beta x} e^{-k_2 z} \quad 2-28$$

$$E_z(z) = -A_2 \frac{\beta}{\omega \varepsilon_0 \varepsilon_2} e^{i\beta x} e^{-k_2 z} \quad 2-29$$

for  $z < 0$ ,

$$H_y(z) = A_1 e^{i\beta x} e^{k_1 z} \quad 2-30$$

$$E_x(z) = -iA_1 \frac{1}{\omega \varepsilon_0 \varepsilon_1} k_1 e^{i\beta x} e^{k_1 z} \quad 2-31$$

$$E_z(z) = -A_1 \frac{\beta}{\omega \varepsilon_0 \varepsilon_1} e^{i\beta x} e^{k_1 z} \quad 2-32$$

where  $k_i = k_{z,i}$  ( $i=1,2$ ) is the perpendicular component of wave vector to the interface of two media and the amplitude modulations are  $A_1$  and  $A_2$  in the medium 1 and 2 respectively.

The reciprocal vector,  $\hat{z} = 1/|k_z|$ , shows the evanescent decay length of fields perpendicular to the interface.

According to continuity of  $H_y$  and  $\varepsilon_i E_z$ , it is found that  $A_1=A_2$  and:

$$\frac{k_2}{k_1} = -\frac{\varepsilon_2}{\varepsilon_1} \quad 2-33$$

In addition, the  $H_y$  needs to satisfy the TM wave equation, Eq. Then the TM mode wave equation from the Eq. (2-14) obtains,

$$\frac{\partial^2 H_y}{\partial z^2} + (k_0^2 \varepsilon - \beta^2) H_y = 0 \quad 2-23:$$

$$k_1^2 = \beta^2 - k_0^2 \varepsilon_1 \quad 2-34$$

$$k_2^2 = \beta^2 - k_0^2 \varepsilon_2 \quad 2-35$$

From Eq. (2-34) and Eq. (2-35), the dispersion relation of SPPs propagating at the metal/dielectric interface can be obtained:

$$\beta = k_0 \sqrt{\frac{\varepsilon_1 \varepsilon_2}{\varepsilon_1 + \varepsilon_2}} \quad 2-36$$

The similar analysis of TE surface mode demonstrates that the surface modes do not exist for TE polarization. So there is only excitation of surface modes for incident light with TM polarization [36].

The surface plasmon polaritons at the planar metal/dielectric interface cannot be excited through incident light, however momentum transferring from incident light to surface Plasmon polaritons (SPPs) inside the light line can be achieved by adding a periodic structure at the interface. The lattice wave vector can compensate the difference between incident light and surface wave momentum which satisfies momentum matching requirement. Two common methods are used to achieve this goal: first, using prism and second, surface engineering using different array apertures at the metal/dielectric interfaces. In

general, two different geometries are designed for prism coupling; Kretschmann [37] and Otto [38] configurations which are known as attenuated total reflection (ATR) method in optics. Both prism schematic diagrams are shown in figure (2.2).

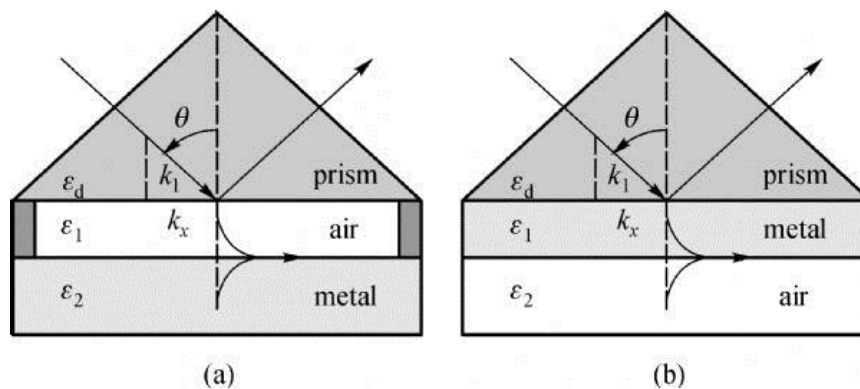


Figure 2.2 Using prism to couple incident light with SPP; (a) Otto (b) Kretschmann configuration [39].

The surface engineering is another method to excite SPPs with periodic nanostructures at the metal/dielectric interfaces. The wave vector of periodic structure can serve to fulfill the momentum matching condition and transfer non-radiative SPP modes to radiative ones inside the light line at the interface, (figure 2.3). The phase matching condition can fulfill in presence of periodic nanostructure with lattice constant  $a$ ,

$$\beta = k \sin \theta \pm v g$$

2-37

Here  $g = \frac{2\pi}{a}$  is the reciprocal vector of the lattice and  $v = 1, 2, 3 \dots$  is an integer correspond to the order of SPP mode [36].

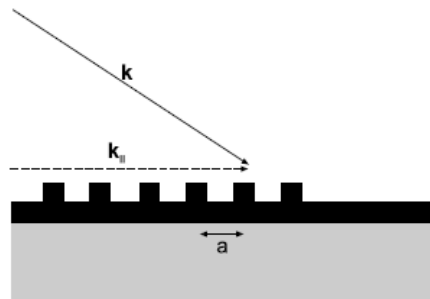


Figure 2.3 Momentum matching condition on the corrugated interface [36].

### 2.1.2 The Effective parameters on coupling strength of plasmonic nanostructures

The array of aperture exhibits high transmission efficiency rather than the single hole with similar area of total small holes, this so-called extraordinary transmission (EOT). The condition of SPP excitations depends on various parameters which gives different coupling strengths and extraordinary transmission through plasmonic nanostructures. In this section, the key parameters of coupling at the metal/dielectric interfaces are briefly explained.

#### 2.1.2.1 Material types in Plasmonic Nanostructure

Noble metals are generally appropriate candidates in plasmonic devices especially working in visible frequencies of the electromagnetic spectrum.

Increasing absorption, is related to the imaginary part of metal permittivity, is resulting in decreasing intensity and linewidth broadening of transmission peak. The skin depth and the absorption length are two main parameters determining coupling strength at the meta/dielectric interfaces. Most common metals are Au, Ag and Cu which support the SPPs' excitation and the EOT. Cr and Ni exhibit large absorption so very low transmission and coupling strength. Al suffers from very low skin depth which cannot yield strong coupling strength [40-41]. The transmission spectra of different metals are shown in the figure (2.4). Besides noble metals, other materials also show the excitation of SPPs mode for example highly doped Si [42], metal-organic conducting polymers [43], VO<sub>2</sub> [44], metal coated VO<sub>2</sub> double layers [45], SrTiO<sub>3</sub> [46], Ga As [47], amorphous SiO<sub>2</sub> [48] and SiC [49]. Generally, a thin conducting film coated on periodic arrays with thickness of the order of skin depth is sufficient to generate the strong coupling and the EOT.

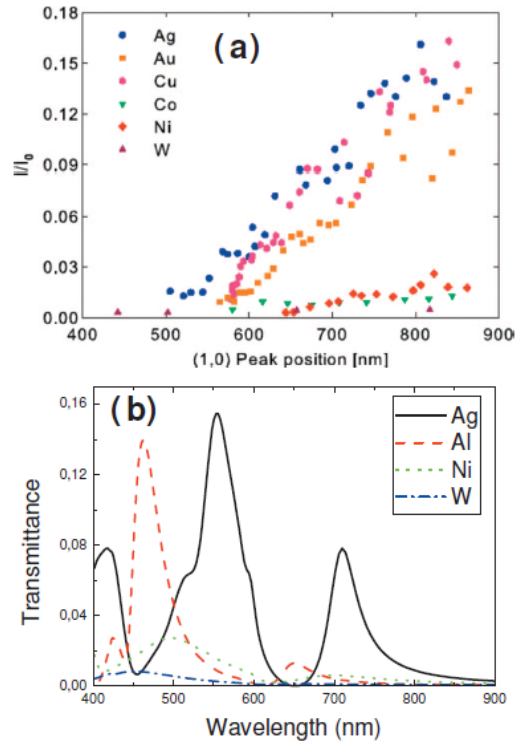


Figure 2.4 the effect of different metals on the EOT through plasmonic nanostructure, (a) experimental [40], (b) theoretical [41] results.

### 2.1.2.2 Size and Shape of Plasmonic Nanostructures

The size of hole has crucial effect on transmission and coupling strength of periodic arrays. Increasing hole diameter results in the enhancement of the intensity and the linewidth of transmission peaks [50-51]. The spectral position of transmission peaks also depends on the size of holes. It was demonstrated a small blue shift of transmission peaks by decreasing hole size [52-53]. Moreover the shape of individual hole in array plays key role in intensity of transmission peaks [54] as well as resulting in polarization anisotropy depending on the direction of propagating waves [55-56]. The pitch

size and aspect ratio of periodic array can also affect the intensity and the spectral position of transmission peaks [57]. The transmittance through periodic plasmonic nanostructure with varying pitch size of rectangular aperture shape ( $260 \times 200 \text{ nm}^2$ ) is shown in the figure (2.5); the measurement was carried out for the two orthogonal polarizations [58].

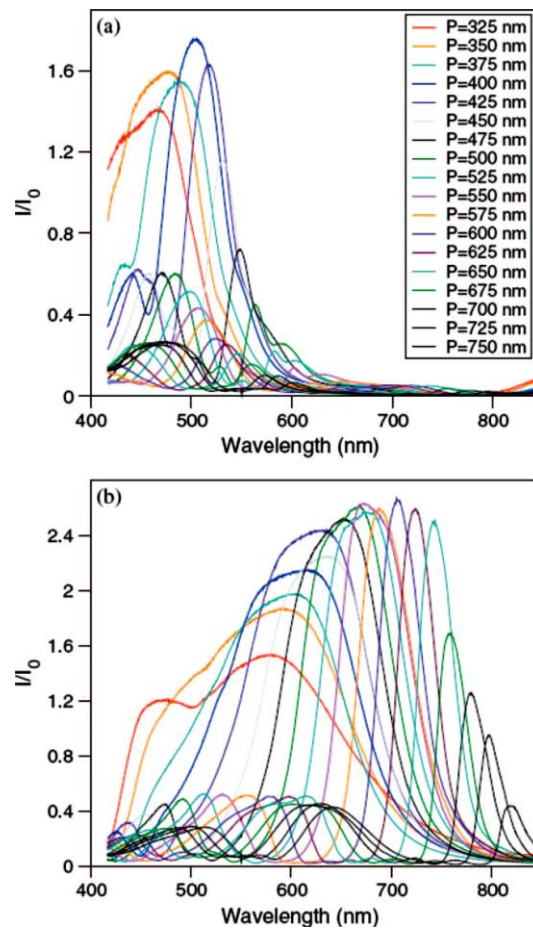


Figure 2.5 the transmission spectra of rectangular aperture with varying period, for the polarization (a) perpendicular to the short edge (b) perpendicular to the long edge.

### **2.1.2.3 The Lattice Finite-Size**

The intensity of transmission peaks and coupling strength can be enhanced by increasing of the numbers of holes in the arrays until reaching the saturation. The hole size plays an important role to compute numbers of holes forming the array for saturation. Larger hole diameter leads to faster transmission saturation [59-61]. The aspect ratio and period of the array are also important for the determination of transmission saturation [62].

There are many other parameters which can affect the efficiency of plasmonic nanostructure such as angular dispersion, metal film thickness, the symmetry role in the dielectric/metal/dielectric layer stack and polarization dependency. All parameters should be considered for fabrication and design of plasmonic nanostructure.

### **2.1.3 Resonance Field Coupling Mechanism**

Nanostructure can be studied through two distinct coupling mechanisms. If the particle distance is sufficiently lower than the plasmon resonance wavelength in the nanostructure then the coupling investigates in the near field regime. On the other hand, the far field coupling would happen when the distance between particles is close to or over the wavelength of the plasmon resonance. Increasing the distance between particles causes the weak coupling strength in

near field coupling regime whereas cavity modes surpassing plasmonic interaction in far field coupling regime.

### 2.1.3.1 The Near-Field Coupling

In plasmonic nanostructure, when the distance between particles is sufficiently larger than the particle size, then we can consider the particle as point dipoles and apply the dipole-dipole approximation for study of the near field plasmonic interaction. In this limit, particles can be aligned in direction of the incident electric field or perpendicular to the field, (Figure 2.6). In the first configuration (figure 2.6a), the restoring force has been decreased by the dipolar electric field of adjacent particles; it suggests that the plasmon resonance shift to lower frequencies. Conversely the restoring force has been reinforced in the second configuration (figure 2.6b), resulting in plasmon resonance shift toward higher frequencies. Therefore, if particles arrange in perpendicular to the incident electric field, much stronger plasmonic coupling can be supposed to occur in near-field interaction.

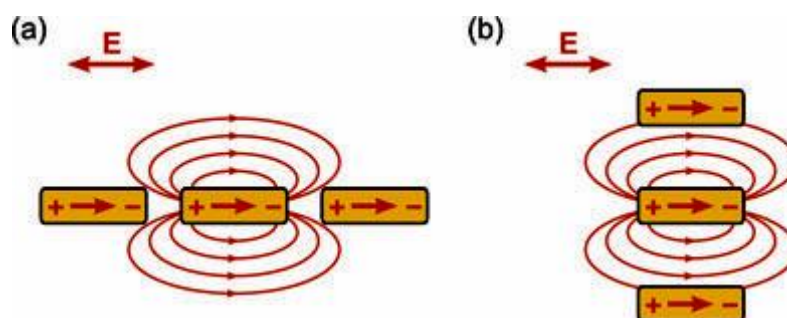


Figure 2.6 the dipole electric field diagram of coupled nanoparticles; (a) parallel (b) perpendicular to the incident electric field [63].

### 2.1.3.1.1 Electric and Magnetic Dipoles

When the dimension size of particles approaches to the distance between particles, it is needed to consider higher order of dipole approximation series which leads to the electric circular current in the nanostructure. In addition, similar to interatomic interaction to form molecules, the plasmonic dipoles can interact to generate energy level hybridization; a symmetric mode with in phase oscillation of two coupled plasmons and an antisymmetric mode for oscillation of coupled plasmons with  $180^\circ$  phase difference, (Figure 2.7). The symmetric mode results in oscillations in higher frequency while the antisymmetric mode oscillates at lower frequency.

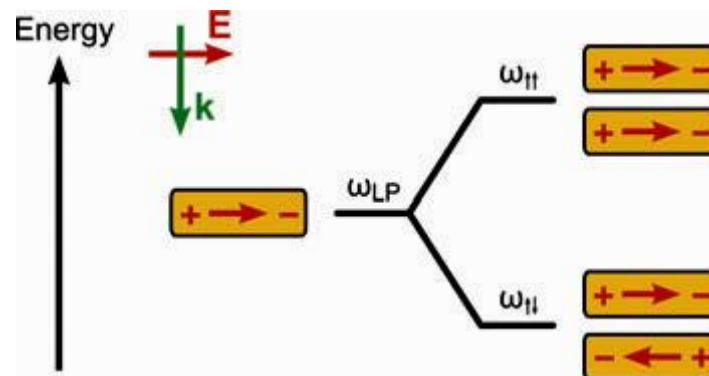


Figure 2.7 the symmetric and antisymmetric mode of the energy level hybridization of coupled plasmonic nanoparticles [63].

The antisymmetric (quadrupole) mode is known as dark or non-radiative mode. However the asymmetric surrounding structure, layers with different thicknesses or using two type dielectric materials, is needed to excite the

antisymmetric mode. The antisymmetric mode exhibits a magnetic moment due to opposite electric current around each pair of particles whereas the symmetric mode points out an electric moment, known as magnetic and electric plasmon modes respectively.

#### **2.1.3.1.2 The Mirror Effect**

The physics of nano particles close to metal layer can be studied in analogy to electrostatic concept of image charges. In this situation, the metal layer effect can be investigated by replacing a nanoparticle with opposite charge distribution on other side of metal film. Two nanoparticles with opposite charge distributions form antisymmetric mode coupling promising the magnetic plasmon moment.

#### **2.1.3.2 The Far-Field Coupling**

Once the distance of particles approaches to the plasmon resonance wavelength, the electrodynamic description should be replaced by quasi-static approximation. In far field interaction, plasmonic nanoparticles behave like Fabry-Perot cavities with resonating mirrors, therefore the phase retardation needs to be considered in calculations.

##### **2.1.3.2.1 The Phase Retardation Model**

The far field investigation of coupled nanoparticles can be done by phase shift model for propagating electromagnetic waves through the system. It is

assumed the resonance cavity condition occurs between nanoparticles then total phase shift in one round trip obtain by multiplying of  $2\pi$ .

The resonance wavelength of cavity defines,

$$\lambda_N = \frac{2n_{cav}d}{(N+1) - \frac{\Delta\phi_{refl}}{\pi}} \quad 2-38$$

$d$  is cavity length and  $n_{cav}$  is the refractive index of cavity medium.  $N$  is an integer and  $\Delta\phi_{refl}$  is the phase shift for reflection from a mirror, if the reflected surface is a plasmonic nanostructure the phase shift depends on wavelength as  $\Delta\phi_{refl}(\lambda)$ .

The wavelength-dependent phase shift can be obtained by driven harmonic oscillator model for the excited plasmonic system,

$$\ddot{r} + \gamma_{LP}\dot{r} + \omega_{LP}^2 r = -\frac{e}{m_e} E_0 e^{-i\omega t} \quad 2-39$$

The plasmon damping is  $\gamma_{LP}$  and  $\omega_{LP}$  is the localized plasmon resonance frequency. It is assumed that the incident electromagnetic wave  $E(t) = E_0 e^{-i\omega t}$  is an external driving force on the electron in the plasmonic nanostructure and it can excite the surface plasmons. Then the solution of Eq. (2-39) is,

$$r(t) = \frac{1}{\omega^2 - \omega_{LP}^2 + i\gamma_{LP}\omega} \frac{e}{m_e} E(t) \quad 2-40$$

The permittivity of plasmonic nanostructure can be derived according to quasi-free electron model. The plasmonic layer is supposed to be

homogeneous; the permittivity leads to lorentzian response at the frequency of localized plasmon resonance,  $\omega_{LP}$ :

$$\epsilon_{LP}(\omega) = 1 - \frac{\omega_P^2}{\omega^2 - \omega_{LP}^2 + i\gamma_{LP}\omega} \quad 2-41$$

$\omega_P$  is the metal plasma frequency.

Therefore the plasmonic refractive index can be acquired in adjacent to an arbitrary dielectric material with refractive index of  $n_d$ :

$$n_{LP}(\omega) = \sqrt{n_d - \frac{\omega_P^2}{\omega^2 - \omega_{LP}^2 + i\gamma_{LP}\omega}} \quad 2-42$$

Using Fresnel equation, the reflectivity of layers of structure can be calculated:

$$R = \frac{R_{12} + R_{23} e^{2ikd}}{1 + R_{12} R_{23} e^{2ikd}} \quad 2-43$$

Where,

$$R_{12} = \frac{n_{cav} - n_{LP}}{n_{cav} + n_{LP}} \quad 2-44$$

And,

$$R_{23} = \frac{n_{LP} - n_{sub}}{n_{LP} + n_{sub}} \quad 2-45$$

Therefore the phase shift of plasmon excitation is obtained by,

$$\Delta\varphi_{exc} = \arctan \frac{Im[R]}{Re[R]} \quad 2-46$$

The refractive index of dielectric layers are  $n_{\text{cav}}$  and  $n_{\text{sub}}$  which plasmonic layer is sandwiched between them [63].

### 2.1.3.3 The Quantum Description of Coupling of Single Emitters with Resonance Filed

Base on quantum electrodynamics, the interaction of single emitters (atom, molecule, quantum dot) with resonance structure like a cavity is known as cavity quantum electrodynamics (cavity QED). The emitter can interact with cavity either coherent or incoherent, (Figure 2.8). The strong coupling of emitter-cavity field occurs at the resonance frequency in the coherent interaction, describing with the coupling constant  $g$ . However the oscillations are gradually dissipated by damping rates through the incoherent interaction leading to the weak coupling regime.

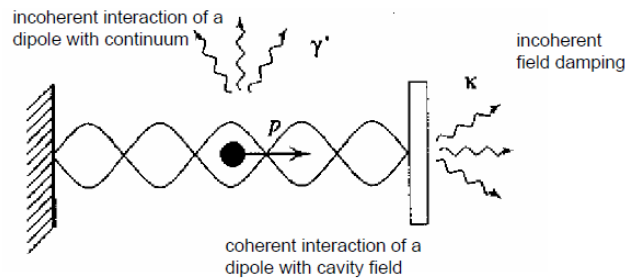


Figure 2.8 the coherent and incoherent interaction of single emitter with electric field of resonance structure [64].

In theoretical calculation, it can be assumed that the emitter as a two-level system interacts with a single cavity mode in the dipole approximation.

In present study, only the strong coupling regime based on dipole approximation is investigated.

First, all damping rates are neglected then the solution of coupled system is given by Jaynes-Cummings-Hamiltonian:

$$H_{JC} = \frac{1}{2} \hbar \omega_0 \sigma_z + \hbar \omega a^\dagger a + \hbar g (a \sigma^+ + a^\dagger \sigma^-) \quad 2-47$$

$\omega_0$  is transition frequency,  $\sigma_z$  is Pauli spin operator,  $\omega$  is the cavity resonance frequency,  $g$  is the coupling constant and  $\sigma^\pm$  is atomic state raising/lowering operator.

This Hamiltonian describes the coupling between states of  $|n, e\rangle$  and  $|n+1, g\rangle$  where  $|n\rangle$  and  $|g\rangle$  are excited and ground states respectively and a photon number state is  $|n\rangle$ .

Therefore Hamiltonian is given by:

$$H_n = \hbar \left( n + \frac{1}{2} \right) \omega \begin{pmatrix} 1 & 0 \\ 0 & 1 \end{pmatrix} + \hbar \begin{pmatrix} -\delta/2 & g\sqrt{n+1} \\ g\sqrt{n+1} & \delta/2 \end{pmatrix} \quad 2-48$$

$\delta = \omega_0 - \omega$  is known as the detuning.

The general state of two-level system is defined by:

$$|\psi\rangle = C_{en}(t) |e, n\rangle + C_{gn+1}(t) |g, n+1\rangle \quad 2-49$$

In resonance, eigenenergies and eigenstates yield as follow:

$$E_{2n} = \hbar \left( n + \frac{1}{2} \right) \omega - \hbar g \sqrt{n+1} \quad 2-50$$

$$E_{2n} = \hbar \left( n + \frac{1}{2} \right) \omega + \hbar g \sqrt{n+1} \quad 2-51$$

$$|2n\rangle = (|e, n\rangle - |g, n+1\rangle) / \sqrt{2} \quad 2-52$$

$$|1n\rangle = (|e, n\rangle + |g, n+1\rangle) / \sqrt{2} \quad 2-53$$

Then the coupled equation of motion for coefficients of  $C_{en}(t)$  and  $C_{gn+1}(t)$  are obtained:

$$\dot{C}_{en} = -i \frac{\delta}{2} C_{en} - ig \sqrt{n+1} C_{gn+1} \quad 2-54$$

$$\dot{C}_{gn+1} = i \frac{\delta}{2} C_{gn+1} - ig \sqrt{n+1} C_{en} \quad 2-55$$

If the state initially is in the upper state, then gets:

$$|C_{en}(t)|^2 = \text{Cos}^2(g\sqrt{n+1}t) \quad 2-56$$

$$|C_{gn+1}(t)|^2 = \text{Sin}^2(g\sqrt{n+1}t) \quad 2-57$$

For  $n = 0$  i.e. there is no photon and only the interaction with vacuum:

$$|C_{e0}(t)|^2 = \text{Cos}^2(gt) \quad 2-58$$

$g$  is known as vacuum Rabi frequency. So there is periodic exchange energy between the emitter and field mode, vacuum Rabi oscillation, unlike the exponential decay in free space of excited atom [65-67].

Figure (2.9) shows the time evolution of emitter inside the resonance structure under different damping rates compared to free space decay.

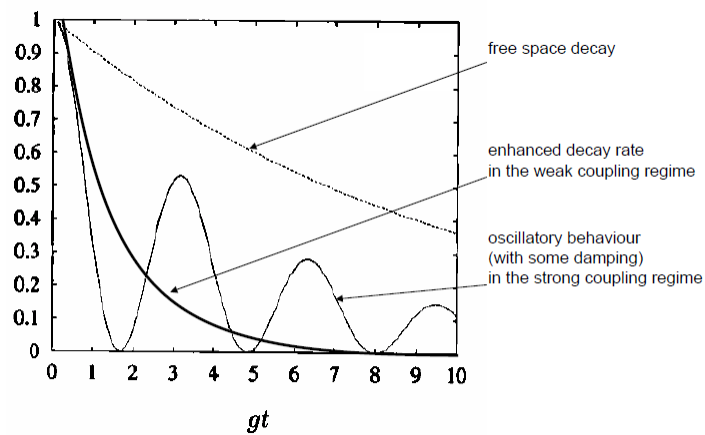


Figure 2.9 Time evolution of interaction of the emitter and resonance structure under different coupling conditions [64].

The normal mode splitting of coupled atom-cavity system occurs in the strong coupling regime, the strong coupling leads to two Lorentzian peaks where the width of peaks related to damping rates and the coupling strength. The strength of coupling is given by the splitting; the frequency difference of the normal mode split.

### 2.1.3.4 The Classical Description of Coupling of Surface Plasmon Polariton and Resonance Field

The coupling of surface plasmon polaritons and resonance structure can be studied in classical electrodynamic, so it is assumed that an emitter close to metal surface behaves like classical Lorentzian oscillator and it can be described with the dynamic of an electron. The electron possesses charge of  $e$  and mass of  $m$ , it is harmonically bound and damped oscillator in the external electromagnetic (EM) field  $E(r, t)$ , and then the equation of motion is given:

$$m(\ddot{r} + \gamma\dot{r} + \omega_0^2 r) = -eE(r, t) \quad 2-59$$

The resonance frequency is  $\omega_0$  and the damping rates are  $\gamma$ .

Considering harmonic EM field  $E(r, t) = E_0 e^{-i\omega t}$  and using dipole approximation for Eq. (2-59), so the steady state solution becomes:

$$r = -\frac{e}{m} \frac{1}{\omega_0^2 - \omega^2 - i\gamma\omega} E_0 e^{-i\omega t} \quad 2-60$$

The dipole moment of electron is defined using Eq. (2-60):

$$p = -er = \frac{e^2}{m} \frac{1}{\omega_0^2 - \omega^2 - i\gamma\omega} E \quad 2-61$$

It is assumed that there are  $N$  dipole moments then the polarization density per unit volume ( $V$ ) becomes:

$$P = \frac{Ne^2}{Vm} \frac{1}{\omega_0^2 - \omega^2 - i\gamma\omega} E \quad 2-62$$

where,

$$\mathbf{p} = \epsilon_0 \chi \mathbf{E} \quad 2-63$$

Thus the macroscopic susceptibility obtains:

$$\chi(\omega) = \frac{Ne^2}{V\epsilon_0 m} \frac{1}{\omega_0^2 - \omega^2 - i\gamma\omega} \quad 2-64$$

The imaginary part of susceptibility gives dissipation and absorption coefficient of material. For limit  $\omega \gg \gamma$  and close to resonance, it obtains:

$$\chi''(\omega) = \text{Im}\chi(\omega) \approx \frac{Ne^2\gamma}{4V\epsilon_0 m\omega_0} \frac{1}{(\omega - \omega_0)^2 + \frac{\gamma^2}{4}} \quad 2-65$$

And the real part:

$$\chi'(\omega) = \text{Re}\chi(\omega) \approx -\frac{Ne^2}{2V\epsilon_0 m\omega_0} \frac{\omega - \omega_0}{(\omega - \omega_0)^2 + \frac{\gamma^2}{4}} \quad 2-66$$

Then the permittivity is given by the susceptibility:

$$\epsilon(\omega) = 1 + \chi(\omega) \quad 2-67$$

The real (n) and imaginary ( $\kappa$ ) part of refractive index are obtained by:

$$\epsilon' = n^2 - \kappa^2 \quad 2-68$$

$$\epsilon'' = 2n\kappa \quad 2-69$$

The SPP dispersion was defined in previous section, Eq. (2-36), as:

$$k = \frac{\omega}{c} \sqrt{\frac{\epsilon_1 \epsilon_2}{\epsilon_1 + \epsilon_2}} \quad 2-70$$

It is assumed that the metal dielectric function  $\epsilon_1$  is constant far away from plasma frequency and involves small range of frequency around resonance frequency  $\omega_0$ . It is supposed that the metal dielectric possesses large negative absolute value compared to the dielectric function of adjacent layer. The numerator of dispersion relation exhibits strong frequency-dependent despite of the denominator. Then the dispersion relation, Eq. (2-70), can be re-written:

$$k^2 = \frac{\omega^2}{c^2} \frac{|\epsilon_1|}{|\epsilon_1 + \epsilon_2|} (1 + \chi(\omega)) \quad 2-71$$

The momentum is defined as the proportion,  $\kappa^2 = k^2 \frac{|\epsilon_1 + \epsilon_2| c^2}{|\epsilon_1|}$ , then:

$$\kappa^2 = \omega^2 (1 + \chi(\omega)) = \omega^2 \left(1 + \frac{A}{(\omega_0^2 - \omega^2 - i\gamma\omega)}\right) \quad 2-72$$

where it is defined  $A = \frac{Ne^2}{V\epsilon_0 m}$  and  $4\pi A^2 = \omega_p^2$ ,  $\omega_p$  is the plasma frequency of free electron gas.

The dispersion relation limit can be considered infinity when  $\kappa \rightarrow \infty$  and zero when  $\kappa = 0$ , the crossing with splitting occurs at the resonance point  $\kappa = \omega_0$  from the dispersion relation.

The size of splitting can be calculated with the assumption of zero damping, so rewrote the Eq. (2-72):

$$\frac{(\kappa+\omega)(\kappa-\omega)}{\omega^2} = \frac{A}{(\omega_0+\omega)(\omega_0-\omega)} \quad 2-73$$

It is assumed  $\omega, \kappa \rightarrow \omega_0$  then  $(\kappa+\omega) \sim 2\omega_0$ ,  $(\omega_0+\omega) \sim 2\omega_0$  and  $\omega^2 \sim \omega_0^2$ :

$$(\kappa - \omega)(\omega_0 - \omega) = \frac{A}{4} \quad 2-74$$

The Eq. (2-74) results in two solutions; two normal modes:

$$\omega_{\pm} = \frac{\kappa}{2} + \frac{\omega_0}{2} \pm \frac{1}{2} \sqrt{A + (\kappa - \omega_0)^2} \quad 2-75$$

The two solutions approximately approach the light line of the SPP in very large and small limit of  $\kappa$ . On the other hand, large value of  $A$  and closer to the resonance  $\kappa=\omega_0$  lead to greater deviation of dispersion relation from the light line. The normal-mode splitting results from the energy difference of two modes  $\omega_+$  and  $\omega_-$  at the resonance point  $\kappa=\omega_0$  similar to the vacuum Rabi splitting in the quantum description. It is given  $\omega = \omega_0 \pm \sqrt{A}/2$  at the resonance condition, so the normal-mode splitting becomes:

$$\Omega = \sqrt{A} = \sqrt{\frac{N}{V}} \frac{e}{\sqrt{\epsilon_0 m}} \quad 2-76$$

Therefore the splitting width directly depends on the square root of the density of number of emitters. It is noteworthy that the splitting of frequency implies to the existence of dynamic in the system and time evolution at frequencies of splitting, here it means the coherent exchange of energy between SPP field and emitters.

### 2.1.3.5 The SPP-Emitter Strong Coupling with Damping Rates

The complete dispersion relation, equation (2-72), is:

$$\kappa^2 = \omega^2 \left( 1 + \frac{A}{(\omega_0^2 - \omega^2 - i\gamma\omega)} \right)$$

To find the solution again the same approximations are applied,  $(\kappa+\omega) \sim 2\omega_0$ ,

$(\omega_0+\omega) \sim 2\omega_0$  and  $\omega \sim \omega_0$ :

$$(\kappa - \omega)(\omega_0 - \omega - i\gamma/2) = \frac{A}{4} \quad 2-77$$

Therefore,

$$\omega_{\pm} = \frac{\kappa}{2} + \frac{\omega_0}{2} - i\frac{\gamma}{4} \pm \frac{1}{2} \sqrt{A + (\kappa - \omega_0 + i\gamma/2)^2} \quad 2-78$$

At resonance:

$$\omega_{\pm} = \omega_0 - i\frac{\gamma}{2} \pm \frac{1}{2} \sqrt{A - \frac{\gamma^2}{4}} \quad 2-79$$

Thus, the damping results in the decrease of Rabi Splitting width.

The loss of SPP can be considered in calculation by replacing  $\kappa$  with  $\kappa - i\gamma_{SPP}/2$

and then two normal modes at resonance are obtained:

$$\omega_{\pm} = \omega_0 - i\frac{\gamma}{4} - i\frac{\gamma_{SPP}}{4} \pm \frac{1}{2} \sqrt{A - \left(\frac{\gamma}{2} - \frac{\gamma_{SPP}}{2}\right)^2} \quad 2-80$$

In fact Rabi splitting can be easily observed only if the difference in the real part of energy, the square root term, is bigger than the width of the new modes,  $\frac{\gamma}{2} + \frac{\gamma_{SPP}}{2}$ , it means:

$$\sqrt{A - \left(\frac{\gamma}{2} - \frac{\gamma_{SPP}}{2}\right)^2} > \frac{\gamma}{2} + \frac{\gamma_{SPP}}{2} \rightarrow A > \frac{\gamma^2}{2} + \frac{\gamma_{SPP}^2}{2} \quad 2-81$$

Thus the strong coupling condition is:

$$\frac{Ne^2}{V\epsilon_0 m} > \frac{\gamma^2}{2} + \frac{\gamma_{SPP}^2}{2} \quad 2-82$$

The strong coupling occurs where the splitting is larger than modes' width; however some modal broadening may exist in the experimental measurement which restricts theoretical calculations. Similar calculations would be reliable for the strong coupling in photonic cavities and plasmonic microcavities [67-68].

### 2.1.3.6 The Strong Modal Coupling from Plasmonic Microcavities

In 1992, the first strong modal coupling was reported between cavity mode and a two-level atom, demonstrated Rabi splitting of normal modes [69]. The cavity was designed to exhibit the same resonance frequency as the atomic transition. There are several key factors to recognize the strong coupling and periodically energy exchanging between cavity and a single emitter like an atom,

- The coupling strength  $g$ ; depending on the electric field inside the cavity and the dipole moment of the excited atom state
- Losses inside the cavity for e.g. mirrors' loss
- Losses of single emitters: spontaneous emission of the atom

The modal splitting occurs when two modes of the same energy are coupled around the common resonance frequency. The coupling strength determines the size of splitting, the strong coupling is observed with large coupling strength. The strong coupling of cavity mode and an atom can be generalized to photonic cavity and plasmonic structure in semiclassical viewpoint instead of quantum effect; it means that the quantum emitter still is two-level system described with the Schrödinger equation and the classical electromagnetic field. Here atomic losses can be replaced by the metallic damping frequency for the theory calculation [63].

Thus the SPP is defined as a two-level system with a ground state  $|g\rangle$  and an excited state  $|e\rangle$  where energy of states are  $E_g$  and  $E_e$  and  $E_e > E_g$ . The electromagnetic field of the SPP mode is described by the field amplitude  $E \cos(\omega t) e^{ik \cdot r}$ , the frequency and wave vector of SPP mode are  $\omega$  and  $k$  which given by dispersion relation, Eq (2-70).

The interaction of a two-level system with the field is studied under the standard dipole approximation. Then the ground and excited states are considered as:

$$|g\rangle = \begin{pmatrix} 0 \\ 1 \end{pmatrix} \quad 2-83$$

$$|e\rangle = \begin{pmatrix} 1 \\ 0 \end{pmatrix} \quad 2-84$$

The transition matrices are described with:

$$\sigma_+ = \begin{pmatrix} 0 & 1 \\ 0 & 0 \end{pmatrix} \quad 2-85$$

$$\sigma_- = \begin{pmatrix} 0 & 0 \\ 1 & 0 \end{pmatrix} \quad 2-86$$

The energies of the states are represented with matrices:

$$\sigma_z = \begin{pmatrix} 1 & 0 \\ 0 & -1 \end{pmatrix} \quad 2-87$$

$$I = \begin{pmatrix} 1 & 0 \\ 0 & 1 \end{pmatrix} \quad 2-88$$

Therefore the coupled system can be described with the Hamiltonian:

$$H = \frac{1}{2}E_e(I + \sigma_z) + \frac{1}{2}E_g(I - \sigma_z) + \hbar\Omega_0(\sigma_+ + \sigma_-) \cos(\omega t) \quad 2-89$$

The semiclassical Rabi frequency is  $\Omega_0$ , where it is proportional to the field amplitude and the dipole moment:

$$\Omega_0 = -\frac{d \cdot E}{\hbar} \quad 2-90$$

Then it is assumed that  $\omega_0 \equiv (E_e - E_g)/\hbar$  and the detuning can be obtained by using the rotating wave approximation (RWA):

$$\delta = \omega - (E_e - E_g)/\hbar = \omega - \omega_0 \quad 2-91$$

Also the Hamiltonian becomes under the RWA:

$$H = -\frac{\hbar\delta}{2}\sigma_z + \frac{\hbar\Omega_0}{2}(\sigma_+ + \sigma_-) \quad 2-92$$

The Hamiltonian, Eq. (2-92), can be diagonalized and the eigenvalues are acquired:

$$E_1 = -\frac{1}{2}\hbar\sqrt{\delta^2 + \Omega_0^2} \quad 2-93$$

$$E_2 = \frac{1}{2}\hbar\sqrt{\delta^2 + \Omega_0^2} \quad 2-94$$

Then the generalized Rabi frequency is defined as:

$$\Omega = \sqrt{\delta^2 + \Omega_0^2} \quad 2-95$$

And also it is denoted:

$$\cos \theta = \frac{\Omega - \delta}{\sqrt{(\Omega - \delta)^2 + \Omega_0^2}} \quad 2-96$$

$$\sin \theta = \frac{\Omega_0}{\sqrt{(\Omega - \delta)^2 + \Omega_0^2}} \quad 2-97$$

Therefore the eigenstates are obtained:

$$|1\rangle = -\sin \theta |e\rangle + \cos \theta |g\rangle \quad 2-98$$

$$|2\rangle = \cos \theta |e\rangle + \sin \theta |g\rangle \quad 2-99$$

Or

$$|g\rangle = \cos \theta |1\rangle + \sin \theta |2\rangle \quad 2-100$$

$$|e\rangle = -\sin \theta |1\rangle + \cos \theta |2\rangle \quad 2-101$$

It is assumed that the system is initially in the ground state, so the time-dependent wavefunction becomes:

$$|\Psi(t)\rangle = \cos \theta e^{-iE_1 t/\hbar} |1\rangle + \sin \theta e^{-iE_2 t/\hbar} |2\rangle \equiv \gamma_g(t) |g\rangle + \gamma_e(t) |e\rangle \quad 2-102$$

Using Eq. (2-98) and Eq. (2-99),

$$\gamma_g(t) = \sin^2 \theta e^{-iE_2 t/\hbar} + \cos^2 \theta e^{-iE_1 t/\hbar} \quad 2-103$$

$$\gamma_e(t) = \sin \theta \cos \theta e^{-iE_2 t/\hbar} - \sin \theta \cos \theta e^{-iE_1 t/\hbar} \quad 2-104$$

It is considered the resonance condition with zero detuning,  $\delta = 0$ :

$$|2\rangle = \frac{1}{2} [|e\rangle + |g\rangle] \quad 2-105$$

$$|1\rangle = \frac{1}{2} [-|e\rangle + |g\rangle] \quad 2-106$$

$$E_1 = -\frac{\hbar\Omega_0}{2} \quad 2-107$$

$$E_2 = \frac{\hbar\Omega_0}{2} \quad 2-108$$

And also the time-dependent wavefunction for an initial ground state becomes:

$$|\Psi(t)\rangle = \cos(\Omega_0 t/2) |g\rangle - i \sin(\Omega_0 t/2) |e\rangle \quad 2-109$$

The equation (2-109) demonstrates the Rabi oscillations between the ground and excited states with Rabi frequency,  $\Omega_0$ , in the coupled system. The system oscillates with the generalized Rabi frequency,  $\Omega$ , away from resonance frequency [67].

The modal splitting directly depends on the coupling strength. When the ratio of the splitting and the modes' linewidth is larger than one, the strong coupling is achieved. In fact, intersecting of resonances of the cavity and plasmons is essential to observe the strong coupling in the coupled system. Therefore the coupling appears from an anti-crossing of the resonances where the cavity resonance possesses the detuning around the plasmon resonance [63].

Theoretical and experimental study of the strong modal coupling was done by many groups to achieve large splitting energies. Figure (2-10) shows the results of the strong coupling for the plasmonic microcavity by Chen et al. [70]. The calculated modal anti-crossing with large Rabi-analogue splitting corresponded with the experimental results.

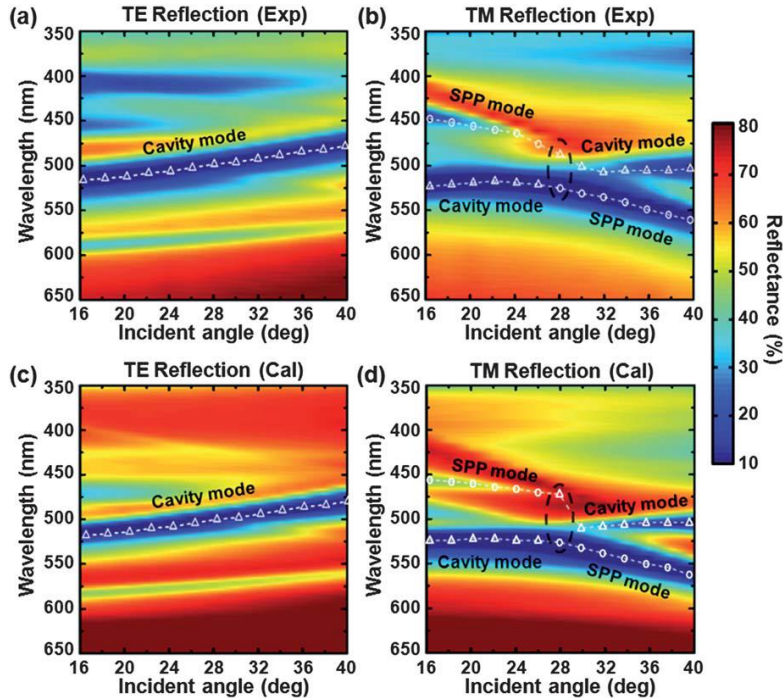


Figure 2.10 the TE and TM (a,b) experimental and (c,d) simulation results of Rabi-like splitting for the plasmonic microcavity. The 2D periodic rectangular aperture array with 320 nm period was integrated onto the Fabry-Perot cavity.

## 2.2 Photolithography Technique

Several lithography techniques have been employed to fabricate periodic array apertures at the interfaces which promise their own specific pros and cons: Ion-beam milling [71], Electron beam lithography [72], Nanoimprint lithography [73] and photolithography [74]. However, beside the precision of fabrication structure, it is important to consider the cost and production convenience in producing a device with dimension suitable for commercial applications.

Ion beam milling and electron beam lithography have a very good precision and the ability to shape different arrays which is indispensable in research work and verification of theoretical concepts; but unfortunately these existing techniques cannot provide a large enough array area and consequently the array area is limited in nano-micro dimensions [75-76]. With the emergent demand, nanoimprint lithography has recently improved considerably to fabricate large area plasmonic arrays although there is still a long haul from research to mass production on metallic layers [77]. In fact the periodic structure can be fabricated cost-effectively using conventional photolithography [78].

### **2.2.1 Optical Lithography**

Generally, optical lithography is a cost-effective lithography technique with capability of meeting all technical requirements. In addition, this technique can provide high throughput with moderate photosensitive resists. But the diffraction limits and substrate reflectivity are the main impediments to employ the optical lithography widely in the fabrication of devices. The diffraction limitation results in the low resolution when the pitch size of pattern is decreased. The resolution directly depends on the wavelength of laser beam and the numerical aperture (NA) of the optics; it would be improved by shortening the wavelength and increasing the NA [79],

$$R = \frac{k_1 \lambda}{NA} \quad 2-110$$

The constant of  $K_1$  is determined by environmental condition of system.

The substrate reflectivity effectively broadens the linewidth due to generating standing waves in the resist and the interference of reflected and incident light at the air-resist interface [79].

In the work, the resist characteristics and fundamental of laser interference will be investigated to acquire basic knowledge of the photolithography steps which will be extensively explained in the chapter 3.

### 2.2.2 Photoresist

Photoresist is a photosensitive material in which the incident light can affect its structure properties. The photoresist is divided into two main positive and negative types regarding to the removal or remaining of the exposed area. Figure (2.12) indicates the process of developing positive and negative photoresist respectively.

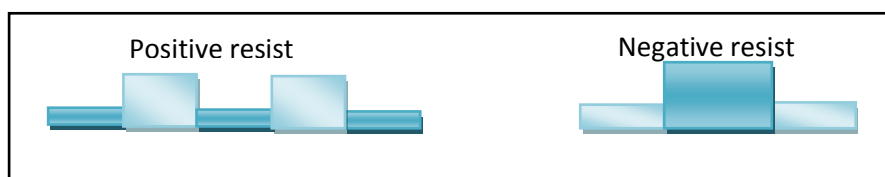


Figure 2.11 The etched pattern fabricated with tow type of photoresist; left: positive, Right: negative.

The photosensitive material may exhibit linear or nonlinear behavior under the light exposure; the sharp edge is resulted in nonlinear resist after illumination

of Gaussian laser beam. The figure (2.13) shows the final pattern shape for both linear and nonlinear resist.

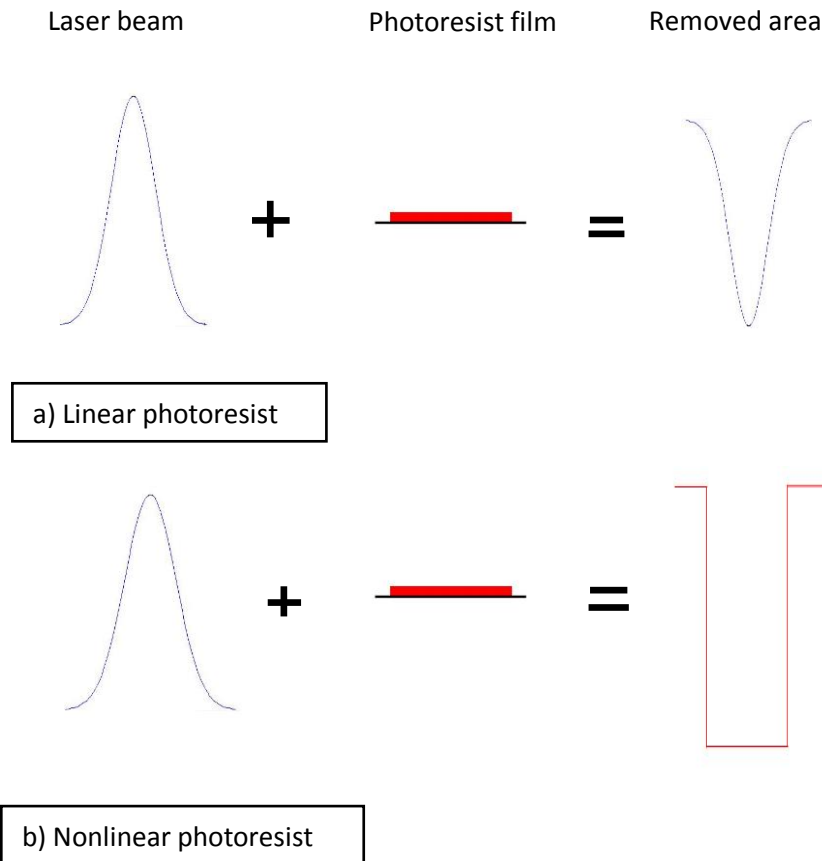


Figure 2.12 The schematic of linear and nonlinear photoresist performance.

Large scale fabrication techniques mostly use high resolution, nonlinear positive photoresist. Since positive photoresists have generally better resolution than negative ones.

Several parameters are to be considered when selecting the proper photoresist for the device fabrication:

- Sensitivity and contrast
- Resist image edge wall
- Resist critical dimension latitude
- Process Compatibility

Furthermore prebake conditions, exposure and development conditions are inseparable to determine the optimum performance of photoresist in the photolithography process [80-81].

### **2.2.3 Laser Interference**

Photolithography is commonly performed in two distinct fabrication procedures; mask lithography and scanning lithography. The pattern is recorded as an amplitude distribution in a lithographic mask and using uniform illumination through the mask to transfer the pattern into the photoresist film in the mask lithography, while the final pattern is designed on photoresist by direct-writing process without using mask in the scanning lithography.

The grating pattern can be fabricated by generating surface profile (surface gratings) or by refractive index variation of the exposed film (volume grating).

Two laser beam interference, Michelson interferometer setup, can be exploited to produce dark and bright fringes as an optical mask in the photolithography technique, figure (2.14). In the interference setup, it is assumed that two equal laser beams with the same amplitude formed the two equal length arms; the local intensity of interference fringes is proportional to individual intensity of each beam.

$$\vec{E}_1(r, t) = \vec{E}_{01} \cos(\vec{k}_1 \cdot \vec{r} - \omega t + \epsilon_1) \quad 2-111$$

$$\vec{E}_2(r, t) = \vec{E}_{02} \cos(\vec{k}_2 \cdot \vec{r} - \omega t + \epsilon_{12}) \quad 2-112$$

$$\vec{E} = \vec{E}_1 + \vec{E}_2 \quad 2-113$$

$$I = \langle \vec{E}^2 \rangle \quad 2-114$$

$$I = I_1 + I_2 + 2\sqrt{I_1 I_2} \cos \delta \quad 2-115$$

$$\delta = \vec{k}_1 \cdot \vec{r} - \vec{k}_2 \cdot \vec{r} + \epsilon_1 - \epsilon_2 \quad 2-116$$

So the maximum intensity, bright fringes, with constructive interference appears when  $\cos \delta = +1$  for  $\delta = 2m\pi$ ,  $m=0,1,2,\dots$ , so the Eq. (2-115) becomes:

$$I = I_1 + I_2 + 2\sqrt{I_1 I_2} \quad 2-117$$

When  $\cos \delta = -1$  for  $\delta = (2m+1)\pi$ , the minimum intensity, dark fringes, with destructive interference occurs and the Eq. (2-115) obtains,

$$I = I_1 + I_2 - 2\sqrt{I_1 I_2} \quad 2-118$$

The pitch size of grating can be tuned by varying the wavelength of laser beam and the angle of two beam interference

$$\Lambda = \lambda/2n\sin\theta \quad 2-119$$

Thus the grating period can be adjusted in wide range proportional to the designed optoelectronic systems.

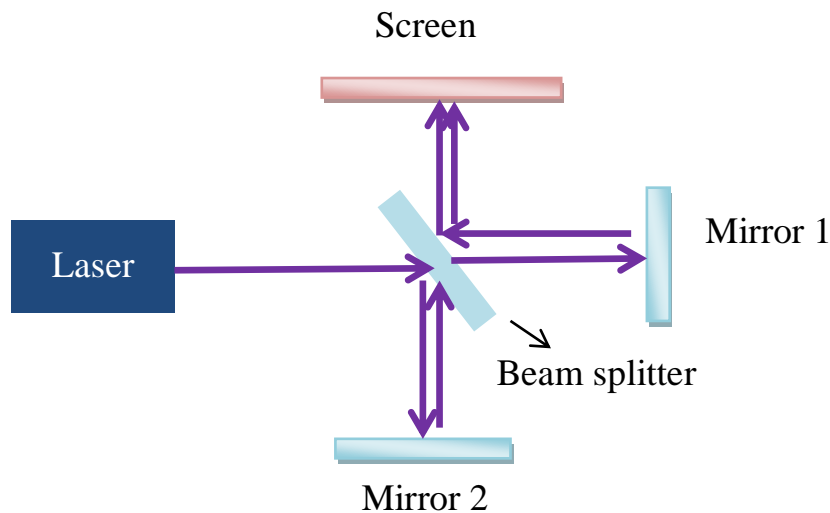


Figure 2.13 The schematic of Michelson interferometer.

In photolithography, the precision of fabricated nanostructure effectively influenced by many factors: the diffraction and scattering effects, the geometry and refractive index of exploited materials in interaction with the incident light, the wavelength, uniformity, coherence and direction of illuminating laser light, numerical aperture of employed optics, the aberration

and misalignment of optical setup and any environmental vibrations. It is essential to consider these factors during fabrication process [82].

## **Chapter 3 Fabrication Technique Fabrication Technique**

In this chapter, the fabrication steps of large area plasmonic nanostructure are described. The fabricated plasmonic nanostructure is a ruled grating, which can be integrated with various optoelectronic devices to improve optical efficiency. First, photolithography technique for grating fabrication will be introduced; followed by preparation details of photoresist film including substrate cleaning, solution preparation and the coating process. Then lithography steps will be explained by means of the use of optical mask and the varying light exposure dose and developing time to optimize for preparing the grating. Thermal evaporation was used for the deposition of thin metal film on the grating. Finally lift-off technique was used to transfer the plasmonic nanostructure to any desire substrate. After all, the measurement and characterization techniques the performance of the plasmonic grating will be described and the related calculation will be discussed.

### **3.1 Photolithography**

Photolithography is a useful technique to fabricate uniform grating pattern, which is commonly used for exciting of surface plasmon polaritons at metal/dielectric interfaces. With this method, a grating mask can be generated

by an interferometer set up towards a thin film of photosensitive material which is known as photoresist.

In the following sections, the fabrication procedure of the grating pattern on the photoresist film and the transfer method of the grating onto dielectric or metal substrate are described.

### **3.1.1 Substrate Preparation**

A clean surface is required to ensure the uniformity of the coated photoresist on glass substrate. Any contamination on glass substrate will give scattering points during light exposure leading to the generation of low quality grating mask having blunt edges and defects. Glass substrates were cleaned with acetone and ethanol to remove organic and inorganic contaminants. Glasses were soaked sequentially in each solvent for 30 minutes in ultrasonic bath. Then they were kept in distilled water in ultrasonic bath for about 30 minutes. At last they were stored in oven with 110°c overnight for drying.

### **3.1.2 Solution Preparation**

Dilution of photoresist and developing solutions for photolithography was needed. Based on the properties of the resist (AP-R 5350), table (3.1), it can provide sufficiently thin film to meet the purpose of present experiment.

Properties / Resist	AR-P	5320	5350
Solids content	%	43	28
Viscosity (25 °C)	mPa·s	220	13
Film thickness at 4000 rpm <small>Semitec CPS 20, uncovered chuck, 2" Si-wafer</small>	µm	5.0	1.0
Film thickness at 6000-2000 rpm	µm	10 (1000 rpm)	0.8 – 1.4
Flash point	°C	42	
Filtration	µm	0.2	
Storage at temperatures	°C	10 - 18	
Guarantee from date of sale	months	6	

Table 3.1 The photoresist, AP-R 5350, properties [83].

In order to have a photoresist film of about 200 nm thickness on glass substrate, the pristine photoresist was diluted by a thinner (AR 300-12) in two different concentration ratios. The photoresist to thinner ratio was 1:1 and 1:2 respectively. Then thin films were prepared by spin-coating method using varied conditions and the thickness was measured. Table (3.2) summarizes spin-coating parameters for thin film preparation. Dilution rate of 1:2 was chosen for the photoresist solution to give the required film thickness.

	Dilution ratio	Thickness	RPM	RAMP	Time(s)
1	1:1	412 nm	2000	3	30
2	1:2	220nm	2000	3	30
3	1:2	188nm	3000	3	30

Table 3.2 Measured thickness of different spin-coated photoresist films.

The developer was diluted by distilled water. The optimum dilution ratio was 1:5 in order to allow reasonable intensity of incident laser light for sample preparation.

### **3.1.3 Photoresist Film Coating**

The spin coating can serve a cheap and fast technique to generate thin films of liquid and solution-processable materials. The spinning speed can be adjusted typically 2000-6000 rotation per minute (rpm) which is high enough to coat various thin film thicknesses. After depositing solution onto the rotating substrate, a thin film of the material is coated over the substrate due to centrifugal forces. The thickness of coated film depends on various parameters such as the spinning speed, the viscosity of the coating material, the temperature of substrate and environment. Despite of the simplicity of coating method, it provides good quality coatings with highly uniform film and free of contaminations [84].

Using the conditions of solution preparation in section 3.1.2, the photoresist was spin-coated on glass substrate with speed of 3000 rpm for 30 seconds. The thickness of photoresist film was around 188 nm. The photoresist film was then pre-baked to remove unwanted solvents and harden for the lithography processes. The baking time took 3 minutes in 100 centigrade.

### 3.1.4 Lithography

Lithography involves two steps; first exposure of light through mask upon the photosensitive film and second immersing resist film into the developer to remove extra photoresist and reveal pattern on the substrate (Figure 3.1).

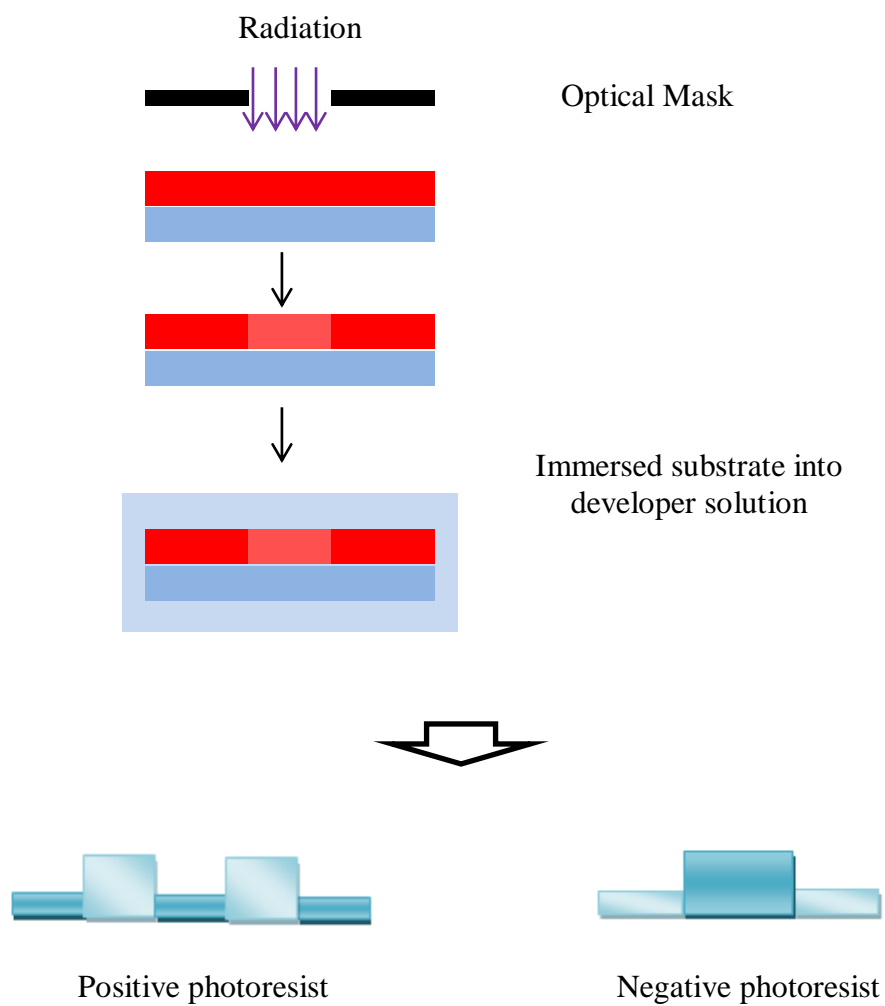


Figure 3.1 The schematic diagram of photolithography process.

### 3.1.4.1 Optical Mask

Michelson interferometer set-up was used to generate optical grating mask on photoresist film. The setup is shown in Figure 3.2. The He-Cd laser provided two tunable emission wavelengths of 442 nm and 325nm. The attenuator was used to reduce the laser intensity and two confocal lenses were to collimate the illuminating light. Besides that, the interferometer setup was aligned such that there were two equal laser beams in each mirror arm with beam-splitter of 50:50 and the optical lengths were equal for both arms. The 442 nm wavelength was used in this experiment as the interfering laser beam due to the absorption spectrum of exerted photoresist, figure (3.2). The interference created dark and bright fringe pattern due to destructive and instructive interferences of the two laser beams, which served as optical mask to transfer ruled grating pattern to photosensitive film. If two beams were not well-aligned to coincide at the interference screen then the optical mask would have low quality and the fabricated grating would not have sharp edge because of shadow edge.

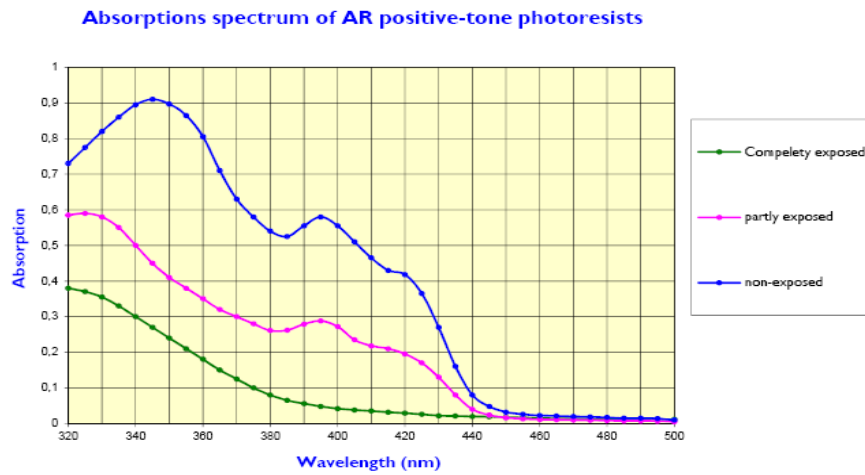


Figure 3.2 The absorption spectrum of AP-R 5350 [85].

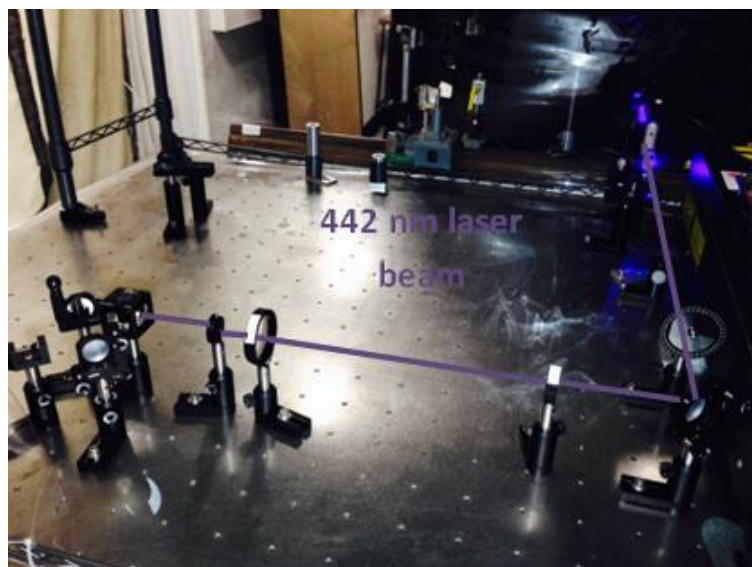


Figure 3.3 The interferometer setup.

It should be noted that the environmental vibration is the most challenging factor for producing desirable grating pattern using the interferometer setup. Noise and vibration will affect the uniformity and quality of the fabricated grating so it is essential to minimize them to the lowest possible level.

### **3.1.4.2 Optimization of Light Exposure Dose and Developing Time**

The time of light exposure on photoresist film depends on several parameters. The thickness of coated film and the material of substrate are the two main factors to produce desired pattern on the photoresist film. Thicker films need more exposure time. The reflectivity of substrate also determines the time of exposure if the thickness of photoresist film are the same. For example silver substrate takes less exposure time rather than glass to create high resolution grating pattern on the photoresist film. The intensity of laser light is another parameter to resolve the time of exposure.

Neither under- or over-exposure of time will not give high quality pattern on the film; instead it may cause low resolution or remove the photoresist completely.

Besides the light exposure time, developing time should also be optimized to produce uniform pattern otherwise the pattern may be removed or not revealed. The optimized of light exposure and developing time are shown in table (3.3) and table (3.4) for two photoresist thickness coated on glass and silver substrate at fixed attenuated laser light intensity.

<b>Glass</b>	<b>Photoresist film thickness</b>	<b>Light exposure time</b>	<b>Developing time</b>
<b>1</b>	220 nm	18 s	4s
<b>2</b>	150 nm	13 s	4s

Table 3.3 Optimized light exposure and developing time for two different photoresist film thicknesses on glass.

<b>Silver</b>	<b>Photoresist film thickness</b>	<b>Light exposure time</b>	<b>Developing time</b>
<b>1</b>	220 nm	14 s	3 s
<b>2</b>	150 nm	8 s	3 s

Table 3.4 Optimized light exposure and developing time for two different photoresist film thicknesses on silver substrate.

### **3.2 Metallic Thin Film Deposition by Thermal Evaporation**

Thermal evaporation is a conventional technique to deposit metal and widely used to fabricate many different devices in the laboratory. In this technique, solid metal are resistively heated to below the boiling point by applying

electrical current in a high vacuum chamber. The metal vapors are gradually deposited and a solid film was formed by condensation of vapors on the substrate surface.

In this experiment a silver film with thickness of 30 nm was deposited on the fabricated grating of photoresist by thermal evaporation.

### **3.3 Grating Characterization**

#### **3.3.1 Scanning Electron Microscopy for Surface Analysis**

Scanning electron microscope (SEM) provides images of sample surface by focusing electron beam and it can give information about topography and composition of fabricated device. In this work SEM was used to determine uniformity and quality of the silver grating during optimization in the fabrication process. Images of the fabricated grating were captured to correlate the results of high and low quality gratings with different reasons. As shown in figure (3.4), long exposure and developing time caused the removal of some regions in the grating pattern on photoresist. On the other hand the grating pattern could not be revealed on photoresist film if the time of exposure and developing was not enough, (figure 3.5). Figure (3.6) shows the effect of vibrations and misalignment of interferometer setup on the quality of the fabricated grating.

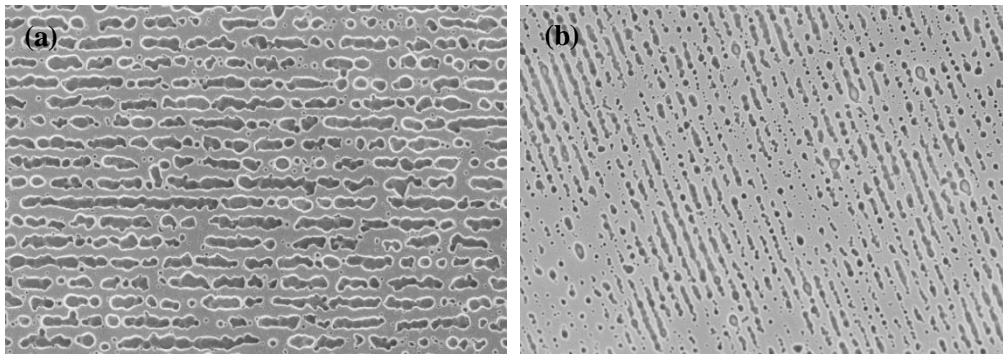


Figure 3.4 Low quality grating patterns due to (a) over-exposure time and (b) overdeveloping time.

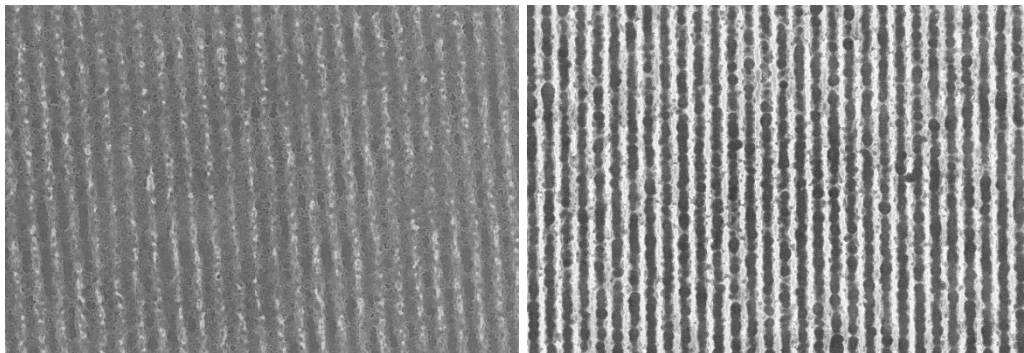


Figure 3.5 Low quality grating patterns due to insufficient time of light exposure and developing.

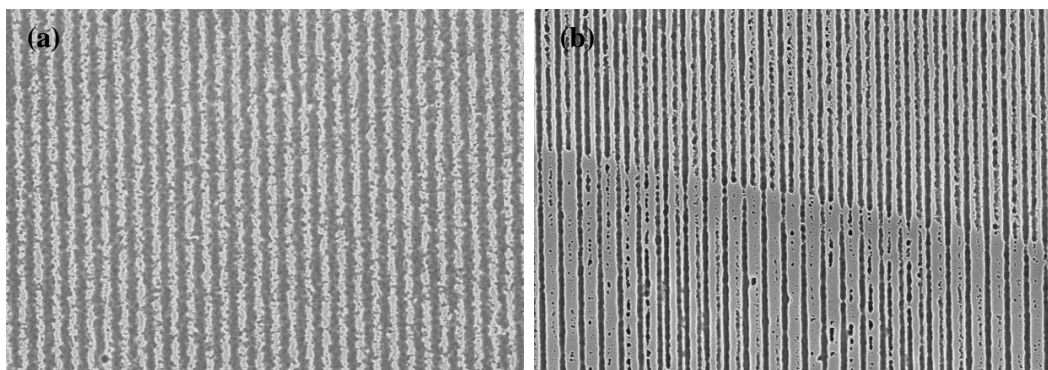


Figure 3.6 Low quality grating patterns caused by (a) environmental vibrations and (b) misalignment of interferometer setup.

Figure (3.7) shows several high quality gratings fabricated with different pitch sizes by tuning the angle between the two beams producing the interference.

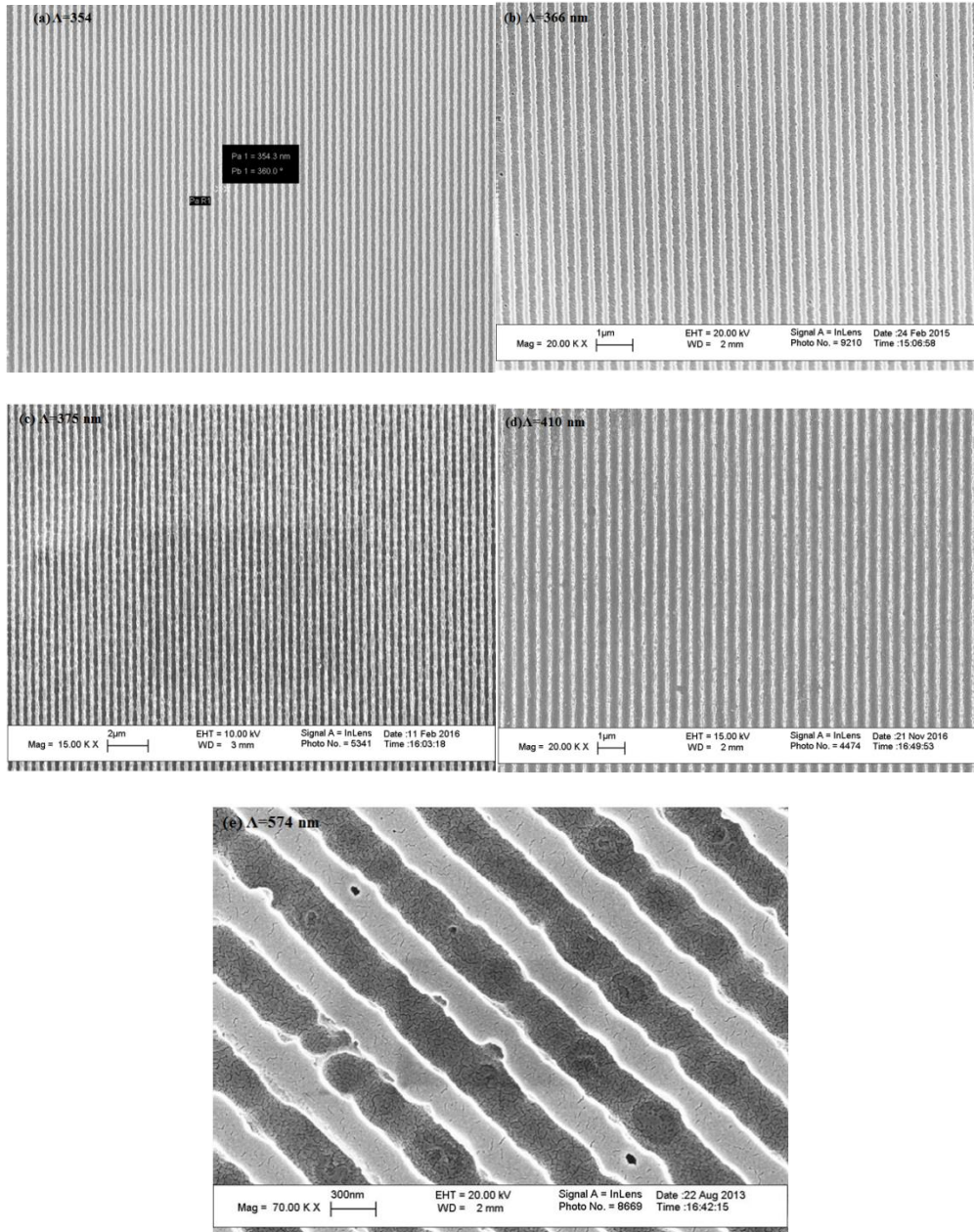


Figure 3.7 Fabricated gratings with different pitch sizes, ( $\Lambda$ ), by photolithography, (a)  $\Lambda=354$  nm, (b)  $\Lambda=366$  nm, (c)  $\Lambda=375$  nm, (d)  $\Lambda=410$ nm, (e)  $\Lambda=574$  nm.

### 3.3.2 Ellipsometric Measurement of SPP Mode

Ellipsometry is an optically non-destructive technique to determine properties of different samples exploiting the characteristics of reflection light. It is sensitive to light polarization and measures polarization changes of reflected light from the surface of the sample (figure (3.8)).

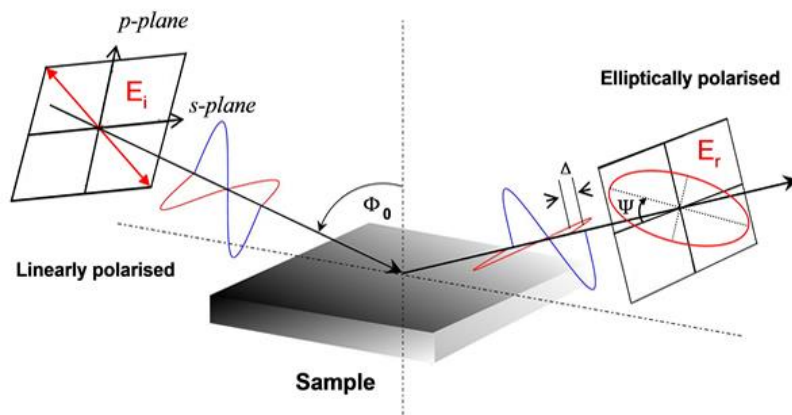


Figure 3.8 Schematic diagram of ellipsometer setup [86].

According to electrodynamics, two orthogonal polarizations of light are s-polarized and p-polarized for electric field, which are perpendicular and parallel to the incident plane respectively. Therefore sample properties can be resolved by measuring polarization changes of reflected light. Ellipsometer measures the ratio of s- and p-reflected light which gives the change of amplitude and phase as follows:

$$\Delta = \Delta_p - \Delta_s \quad 3-1$$

$$\tan \psi = \frac{\left(\frac{E_p}{E_s}\right)_{\text{Reflected}}}{\left(\frac{E_p}{E_s}\right)_{\text{incident}}} \quad 3-2$$

$$\frac{r_p}{r_s} = \tan \psi e^{i\Delta} \quad 3-3$$

Where  $\Delta_p$  is the phase of p-polarized field,  $\Delta_s$  is the phase of S-polarized light,  $\Delta$  is the relative phase change and  $\psi$  is the relative amplitude change,  $E_p$  and  $E_s$  are amplitudes of electric field along p- and s-polarization,  $r_p$  is p-polarized reflection mode and  $r_s$  is s-polarized reflection mode [87].

In this work, ellipsometric measurement was used to determine the change of amplitude and phase of reflected light due to SPP excitation at the interface of air and fabricated metal grating. Measurements were carried out at different incident angles. The change of amplitude in reflected light is shown in figure (3.9a), which is well coincided with the phase change at the same wavelength (around 650 – 750 nm) as shown in figure (3.9b), where the sample was a metal grating with pitch size of 360 nm and 30 nm height.

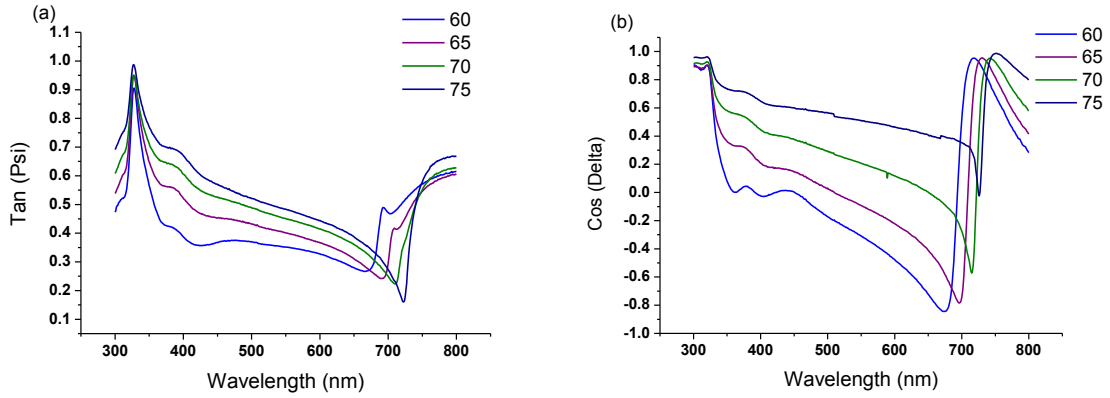


Figure 3.9 Measurement of (a) amplitude and (b) phase change of first mode of SPP at different incident angles.

### 3.3.3 SPP Mode Calculation

The wave vector of surface plasmon polaritons can be calculated with Eq. (2-36) for metal/dielectric interface. For grating interface to excite SPPs, momentum matching condition is given in Eq. (2-37) [88],

$$\beta = k_0 \sqrt{\frac{\epsilon_1 \epsilon_2}{\epsilon_1 + \epsilon_2}} \quad 3-4$$

$$\beta = k \sin \theta \pm v g \quad 3-5$$

Using equations (2-36) and (2-37), the first mode of SPP excitation with a period of 360 nm at varied incident angles can be determined. The figure (3.10) shows calculated results are matched well with experimental ones.

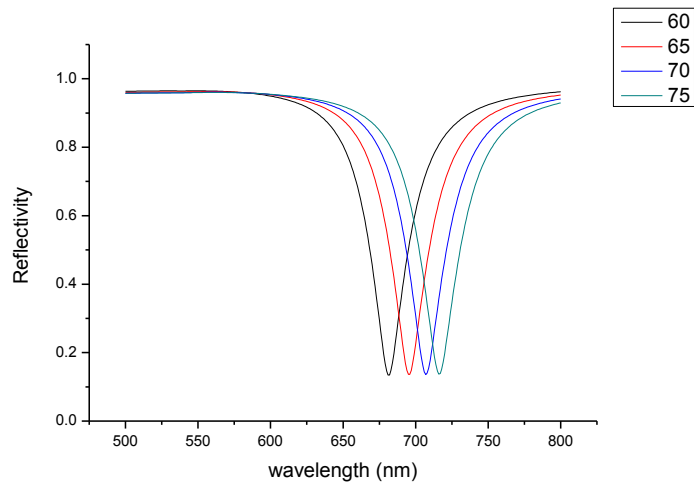


Figure 3.10 The calculation of the first mode of SPP excitation at varied incident angles.

### 3.4 Liftoff Technique

Transferring the metal grating to specific substrate for other applications is needed. The liftoff technique is one of the transferring processes. The metal film was coated on photoresist grating and then the whole device was immersed into the proper solvent to remove extra photoresist. Finally the metal grating on the substrate was completed. The process is shown in figure (3.11). Furthermore it is possible to transfer the fabricated metal grating to soft substrate to produce flexible devices. The flexible metal grating is shown in figure (3.12).

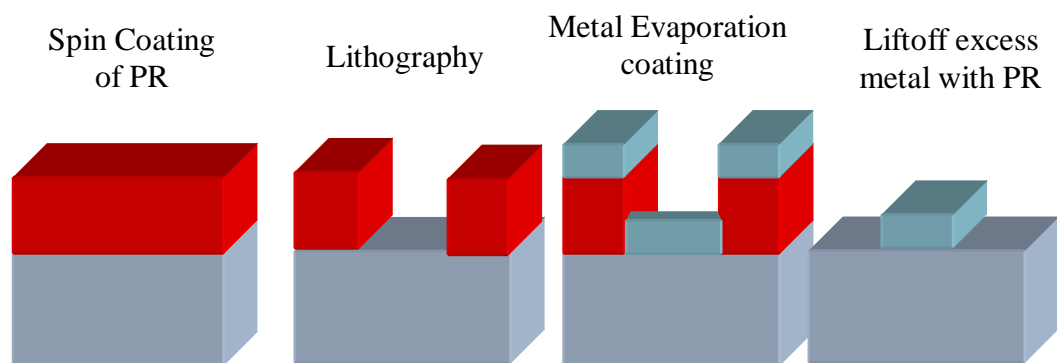


Figure 3.11 Lift-off technique diagram.



Figure 3.12 The flexible fabricated grating on soft substrate.

This technique can be employed to the fabrication of various plasmonic nanostructures with the combination of physical and optical mask in the interferometer set up. For example, via exposing the photoresist film twice or more by rotating the plane of the film square and hexagonal aperture arrays can be prepared.

## **Chapter 4 Plasmonic Microcavities**

In this chapter, the fabrication of plasmonic microcavity is introduced. A large area grating pattern,  $10 \times 10 \text{ mm}^2$ , on top of microcavity structure that allows cavity mode-SPP coupling was prepared. So far the coupling could only be achieved in array of aperture in micro size which is not suitable for sensor application. The photonic cavity can operate as passive or active depending on dielectric medium of cavity. The large area plasmonic cavity can be practically employed in different photonic devices for instance plasmonic lasers [89], biosensors [90-91], metamaterial [92], organic/photonic-plasmonic systems [93-94].

### **4.1 Passive Plasmonic Microcavity**

Passive photonic cavity is fabricated with dielectric medium which the characteristic of material is independent of intensity and wavelength of incident light. It was exerted two different dielectric medium for fabrication of plasmonic microcavity to attain the coupling of the cavity and SPP modes at the interface. First, the thick photoresist film with generated grating pattern is used as spacer for cavity and the plasmonic cavity with inlaid plasmonic nanostructures was fabricated. However the result of coupling was not satisfying and the device could not support high quality and strong cavity mode to generate the modal coupling. Then the second photonic cavity was made by exerting the PMMA (polymethyl methacrylate) as cavity dielectric

medium and the plasmonic grating is separately generated on top of photonic cavity. The second fabricated plasmonic microcavity could successfully demonstrate the strong modal coupling.

#### **4.1.1 Introduction of Exerted Materials**

The Fabry-Perot cavity was designed as photonic cavity and then Mirrors of cavity were thermally evaporated using silver pellets. The fabricated grating pattern was also coated by thin film of silver to support SPP excitation and coupling. PMMA (Microchem 950 PMMA A) was used as passive dielectric medium in photonic cavity. PMMA is transparent organic material with refractive index of 1.48 over the visible spectrum and can serve as high quality cavity medium with low absorption. It can be diluted with chlorobenzene to tune spin-coated thickness as well as controlling of spin-coating speed. The optical properties of used PMMA are shown in figure (4.1).

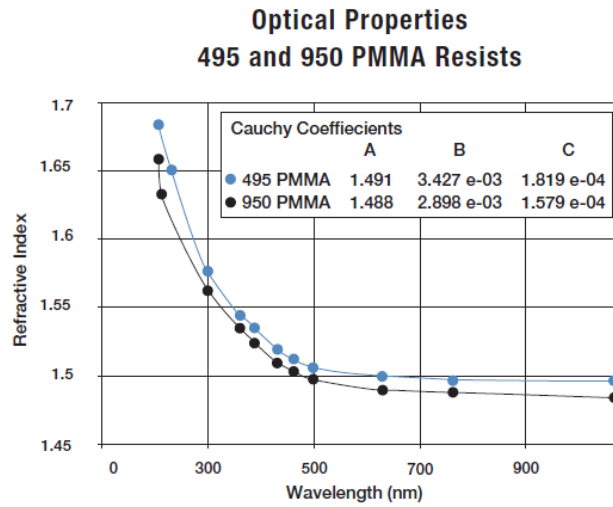


Figure 4.1 Optical properties of the exerted PMMA (polymethyl methacrylate) as dielectric medium of photonic cavity [95].

#### 4.1.2 Structure of Fabricated Plasmonic Cavity

Two different structures were made to achieve the cavity mode-SPP coupling. First, it was designated the cavity without separate dielectric and thick photoresist layer was used as dielectric spacer with the plasmonic grating. Second, the single photonic cavity was fabricated with PMMA as cavity medium and then the plasmonic grating was integrated onto the cavity. The fabricated structures are shown in the Figure 4.2).

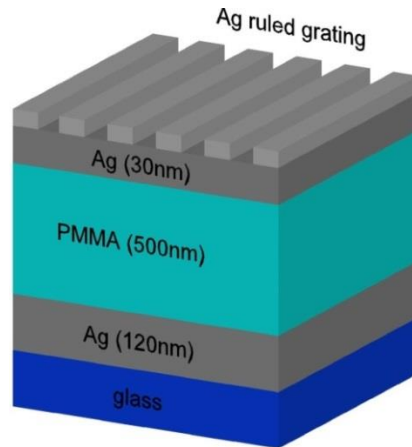


Figure 4.2 The structure of fabricated plasmonic microcavity.

The front and back Mirrors of photonic cavity were deposited by thermal evaporation technique and the intermediate dielectric layer was spin-coated. The ruled metal grating structure was generated on the photonic cavity by photolithography which was explained in chapter 3.

### 4.1.3 Reflection Measurement Analysis for Different Cavity Thicknesses

#### 4.1.3.1 Passive Plasmonic Microcavity with Photoresist Medium

Primarily, the reflectivity of TM (Transverse Magnetic) and TE (Transverse Electric) incident light from the plasmonic microcavity were measured in order to investigate the cavity and SPP mode interaction here. The pitch size of silver grating was around 370 nm with height of 30nm, and the cavity length was varied from 170 nm to 200 nm. As it has been shown in the figure (4.3) the designated structure could not support the cavity mode-SPP coupling

upon the plasmonic microcavities, only the distinct cavity and SPP modes were detected by photometry measurement.

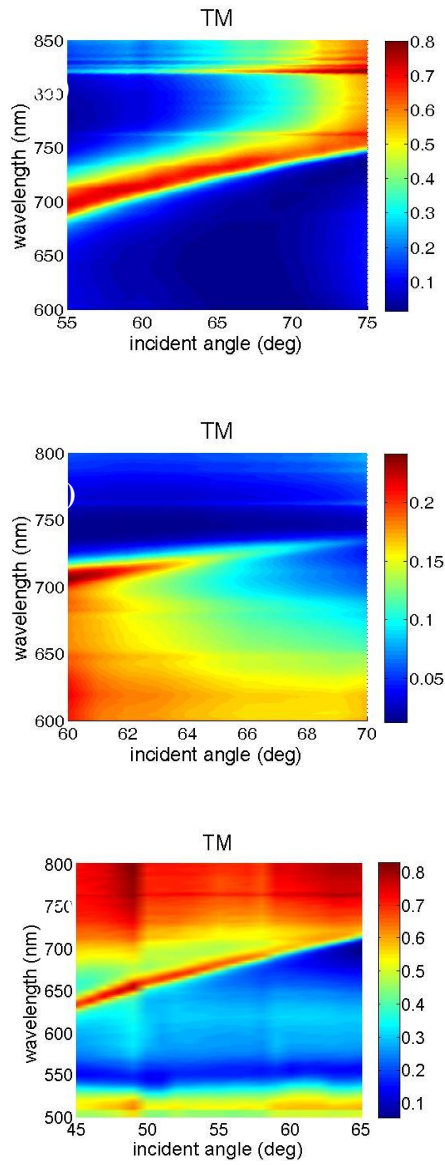


Figure 4.3 (a) cavity length is 200 nm and grating pitch size is 370 nm, (b) cavity length is 190 nm and grating pitch size is 370 nm, (c) cavity length is 170 nm and grating pitch size is 370 nm.

The TM mode of reflection light was measured to determine the cavity mode-SPP coupling base on plasmonic theory. The SPP mode and cavity mode could hardly be recognized in first and second fabricated cavities, figures (4. 3a) and (4. 3b). Although in the third device, the cavity and SPP mode were obvious, however any cavity mode-SPP coupling in the TM reflection light was not demonstrated, figure (4. 3c).

To determine uniformity of large area plasmonic microcavity, we carried out reflectivity measurement in three distinct areas of the third fabricated plasmonic cavity for angles from 54 to 56 degrees. It could be observed that there is no big difference between reflection spectra in figure (4.4).

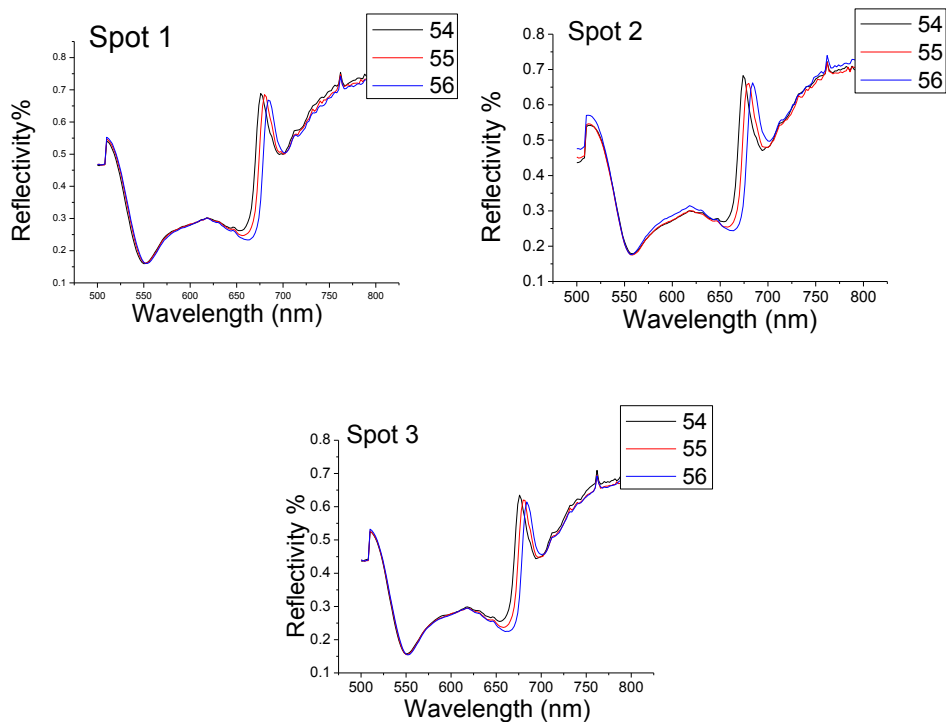


Figure 4.4 the reflectivity measurement of TM mode of three different regions of fabricated plasmonic microcavities for angles from 54 to 56 degrees.

#### **4.1.3.2 Passive Plasmonic Microcavity with PMMA Medium**

The thickness of photoresist film cannot support cavity volume to generate the cavity mode with high quality. To improve cavity modes, the single Fabry-Perot cavity filled with PMMA was fabricated. The front and back silver mirrors were again coated by thermal evaporation technique with thicknesses 30 nm and 120 nm respectively. The PMMA solution was diluted by chlorobenzene with ratio of 1:2 and spin-coated as the intermediate layer of cavity. Thereafter the ruled silver grating was fabricated onto the top mirror of the cavity by photolithography in which the silver grating was made with height of 15 nm and pitch size of 390 nm. The TM reflected light was again measured from different fabricated plasmonic microcavities at the range of angles to determine the cavity-SPP mode coupling at the interface. We made the photonic cavity with different lengths to match cavity mode with SPP mode. The cavity mode and SPP interaction was gradually improved by tuning the cavity length, as shown in the figure (4.5). The first cavity length is around 1  $\mu\text{m}$ , figure (4. 5a), where modes are not clearly recognizable. Then the cavity length was changed to 1.2  $\mu\text{m}$  in which the cavity mode was observed without modal coupling, figure (4. 5b). Finally, the coupling is observed from the plasmonic microcavity with the cavity length of 500 nm, figure (4. 5c). Then the fabrication process was optimized to get better results of strong modal coupling from the plasmonic microcavities. The results show that

strong modal coupling occurs in TM reflection and anti-crossing at 49 degree and the wavelength of 715 nm, as indicated in the figure (4.6).

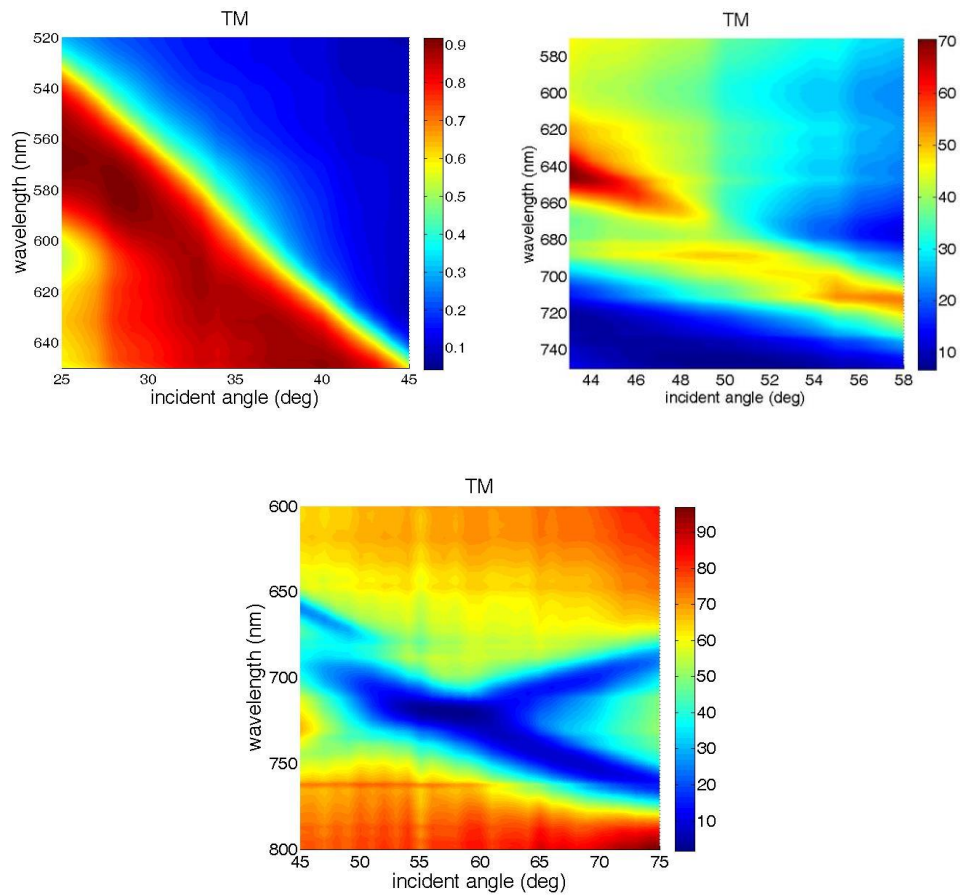


Figure 4.5 The measured reflectivity of TM mode for the plasmonic microcavities with the silver grating period 390 nm and varying cavity length; (a) 1  $\mu\text{m}$ , (b) 1.2  $\mu\text{m}$ , (c) 500 nm.

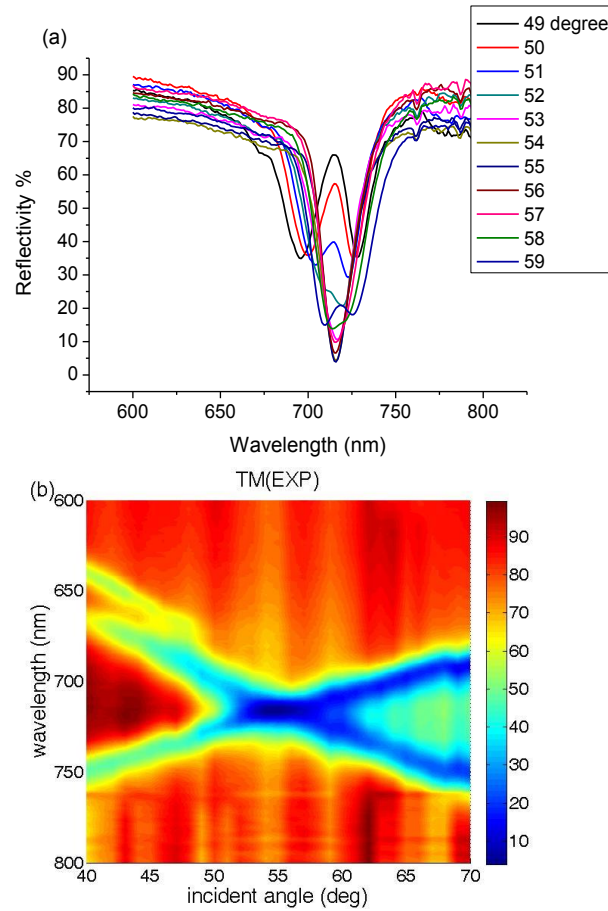


Figure 4.6 Rabi-like splitting at 49 degree (a), the measurement of TM mode coupling of SPPs and cavity modes with anti-crossing at 49 degree and conversional channel from 53 to 57 degree (b).

The reflectivity of TM (Transverse Magnetic) and TE (Transverse Electric) modes with incident light coming from the plasmonic microcavity were measured. The reflectivity of TM polarized incident light is shown in the figure (4.6a), two modes coupled around a common wavelength, exhibiting Rabi-like splitting in the strong coupling regime where the minimum energy gap of upper and lower branches occurred. The reflectivity results show that strong modal coupling occurs in TM reflection from 48 degree with Rabi-like

splitting at 49 degree and wavelength of 715 nm where the splitting energy is minimum value. The mode coupling is generally estimated as ‘strong’ when the ratio of splitting and the mode linewidth is larger than one; here we derive the ratio of larger than one at 49 degree with splitting energy of 78 meV (32 nm linewidth in the spectrum). The range of cavity window spectral and SPP mode excitation can be controlled by tuning the cavity length and the grating period respectively. If both cavity and SPP modes are not sufficiently close in energy, the modal coupling does not occur in the hybrid system. Plasmonic nanostructures generate SPP excitations with strong local field but it suffers from broad linewidth due to high dissipation inside the metal. On the other hand, the cavity mode has narrow linewidth with the weak local resonance field inside the cavity. The hybrid plasmonic microcavity allows the cavity mode and SPPs to couple generating Rabi-like splitting around common wavelength in the strong coupling regime. Therefore there is exchange energy between two resonance modes where the coupled system possesses two modes with the reinforced and improved characteristics; strong local field and narrow linewidth. The modified modes can be employed in various applications especially in polariton laser fabrication to decrease pumping threshold and in biosensor to detect small molecules with red shift of SPP excitation wavelength due to refractive index variations. The mode coupling is from 49 to 57 degree. This extended channel of mode conversion could be employed for mode selection of photonic devices to minimize losses in the visible spectral range, figure (4.6b). Besides the calculation of SPP and cavity modes

was carried out independently to verify that the experimentally observed SPPs and cavity modes are in fact originated from the assumed sources, the metal grating and microcavity, (figure (7a, b)).

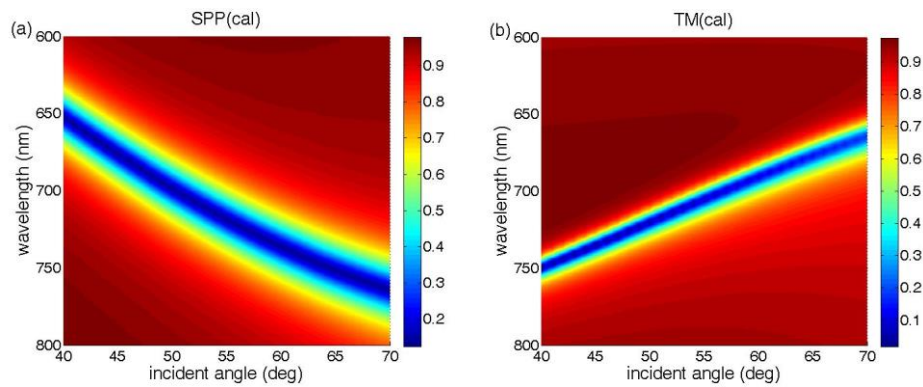


Figure 4.7 Calculation of (a) SPP modes and (b) cavity modes for angles from 40 to 70 degree.

In addition, the measurement of TE mode reflectivity revealed that there was no coupling with SPP mode excitation verifying the theoretical claim on the absence of transverse electric field at the surface, figure (4.8).

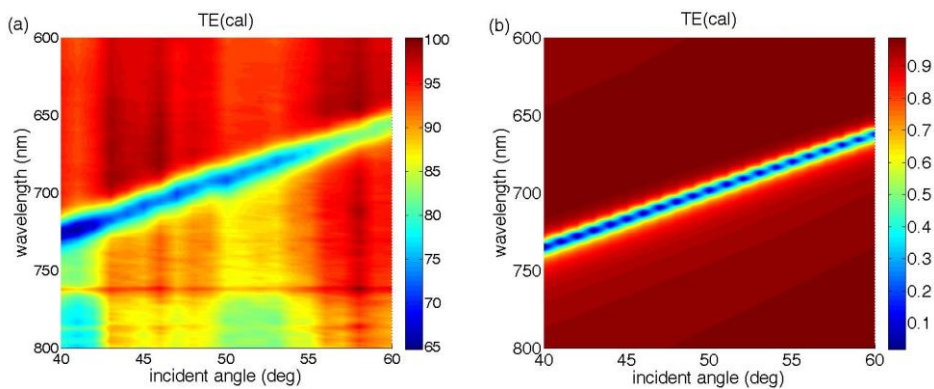


Figure 4.8 The TE mode reflection from designated cavity structure; (a) experimental and (b) calculation result.

The fabrication process needs special meticulous attention to avoid the surface deflection. The solution for the developing step of lithography can be dissolved the dielectric medium of cavity, therefore if it penetrates underneath the front mirror of cavity, low quality plasmonic microcavity would be obtained. The surface quality of low quality cavity is shown in the figure (4.9).

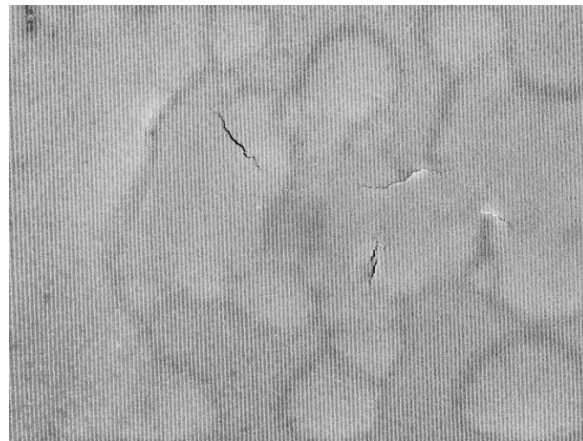


Figure 4.9 The low quality plasmonic microcavity because of the penetration of developing solution.

#### **4.2 Active Plasmonic Microcavity**

The strong coupling regime was analyzed by many research groups in different hybrid plasmonic-organic/inorganic frameworks [96-97]. Hence the modal coupling of hybrid plasmonic cavity was abundantly studied. The cavity mode and Surface Plasmon Polariton (SPP) coupling results Rabi-like splitting similar that of quantum electrodynamic phenomenon where a single emitter interact with the resonant field of the resonator [98-101]. The modal splitting occurs when two modes of the same energy are coupled around the

common resonance frequency and the coupling strength determines the size of splitting. It can be acknowledged fitting and controlling energy distribution or exchange pathway to control device characteristics in the strong coupling regime [102-105]. However optoelectronic devices have gradually replaced instead of conventional optical and electrical devices in many applications. Thusly it sounds essential to improve fabrication techniques and extend exerted material to get optimum performance beside cost-effective of mass production. Having this in mind, the interface of dielectric and conductor in optoelectronic devices are essential to explore the plasmonic behavior at various interfaces. Dielectric can be as inorganic and organic; its selection depends on their attributes. Presently organic materials are particularly attractive due to their long exciton lifetime which makes strong modal coupling in interaction with surface plasmon polaritons probable [106-107]. To provide strong coupling regime, utilized organic material ought to serve limited transition linewidth [108-109]. Individuals ordinarily utilize J-aggregate molecules to fulfill strong coupling conditions with organic materials at plasmonic interfaces [110-113]. But J-aggregate molecules require special environmental prerequisites to function properly and maintain stable interaction. In this study, we used small florescent molecules to investigate the strong modal coupling at the organic/plasmonic interface. We focus on the strong modal coupling of plasmonic microcavity using florescent organic material, EY51 (Rubrene-like), in dielectric medium of photonic cavity. We believe the interaction of active medium cavity and plasmonic nanostructure

has not been studied before. We observed the anti-crossing with enormous Rabi-like splitting at cavity mode-SPP coupling in large area hybrid plasmonic microcavity. We also investigated the absorption impact on the coupling strength of various intermediate layer lengths of cavity. Furthermore, the photoluminescence (PL) emission measurement was carried out for plasmonic and photonic microcavity and acquired higher intensity of PL emission in the plasmonic cavity than photonic one. The device was manufactured with conventional photolithography to provide the required practicality and cost-efficiency of mass production for various applications [114-115].

#### **4. 2. 1 Active Plasmonic Microcavity Structure**

We exploited conventional photolithography technique to fabricate large area plasmonic nanostructure. The ruled grating pattern was fabricated on glass substrate in large area, ( $10 \times 10 \text{ mm}^2$ ), and it can be made in larger area, several centimeters, by using proper expanding/collimating setup. The pitch size of grating was about 360 nm with the height of 20 nm. The scanning electron microscopy was used to determine the surface quality and uniformity of the fabricated grating pattern, figure (4.10). Subsequently, the ruled metal grating was integrated into photonic cavity to form the hybrid plasmonic microcavity. The silver layers with 45 nm and 120 nm thicknesses were thermally evaporated as front and back mirrors of photonic cavity respectively. The intermediate dielectric layer of cavity was a thin film of Rubrene on front

mirror and followed by PMMA layer; both dielectric layers were spin-coated.

Figure (4.10) shows the device configuration.

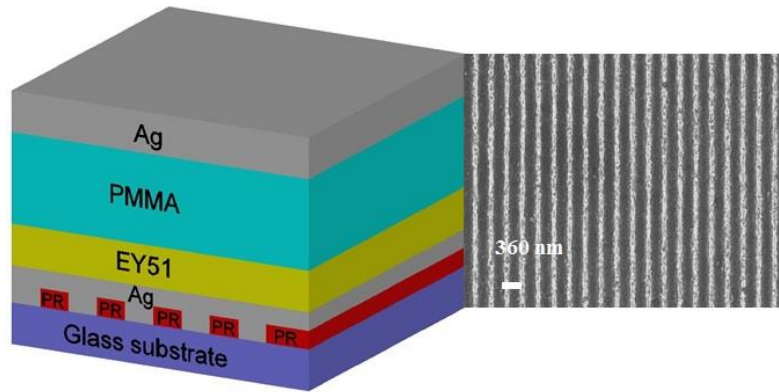


Figure 4.10 The hybrid plasmonic microcavity configuration and the SEM image of grating surface quality.

#### 4. 2. 2 The Material Characterization of Intermediate Dielectric Layer of Photonic Cavity

PMMA was the main dielectric medium of photonic cavity. A thin layer of florescent material was spin-coated to investigate the cavity mode-SPP coupling of active plasmonic microcavity. In this research, the organic molecules of Rubrene were used in the cavity. The molecular structure of Rubrene is shown in figure (4.11).

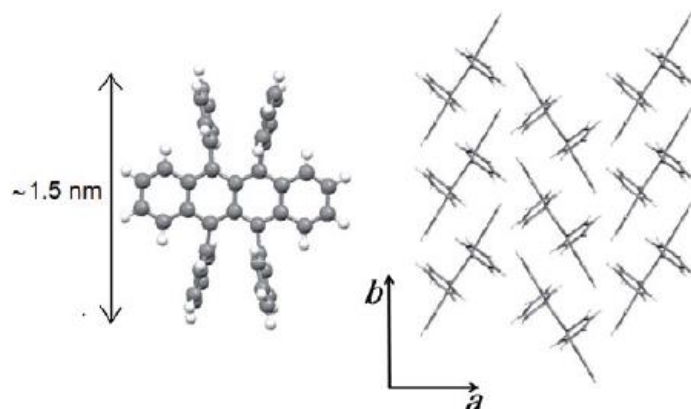


Figure 4.11 Molecular structure of Rubrene (116).

Rubrene is a yellow fluorescent organic material and it demonstrates photoluminescence (PL) emission in the range of yellow color of visible spectrum. The PL emission spectrum of pristine film of Rubrene on the glass substrate was shown in the figure (4.12).

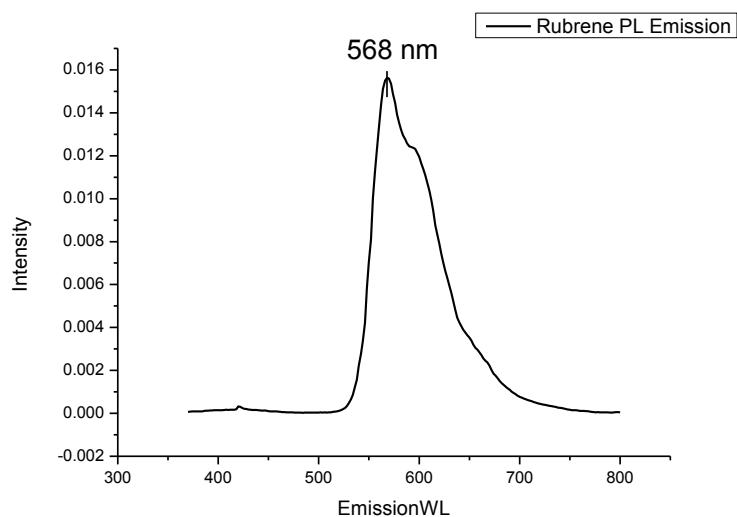


Figure 4.12 The PL emission spectrum of Rubrene.

### 4. 2. 3 Results and Discussion

The TM (Transverse Magnetic) reflected mode was measured to evaluate cavity mode-SPP coupling at the interface. The results show that an extremely strong cavity mode-SPP coupling at the incident angle of 50 degrees and this is obtained with the fabricated plasmonic microcavity with length of 630 and the PL coated thickness is roughly 30 nm, (cavity (a)). The anti-crossing has large Rabi-like splitting around common resonance wavelength, 619 nm, of the two coupled modes. The splitting energy is 280 meV (85 nm linewidth), (figure (4.13a)). In comparison with the passive plasmonic microcavities, using fluorescent material film resulted in a considerable improvement of the coupling quality and strength and created a larger modal splitting on the coupled system.

To investigate the absorption effect on the coupling strength, we fabricated two more hybrid plasmonic microcavities with cavity lengths of 600 nm and 670 nm, the thicknesses of fluorescent material are 50 nm and 80 nm, respectively. It was clearly observed that increasing the PL film thickness leads to reduction of the coupling strength of the hybrid plasmonic systems. The anti-crossing was occurred with splitting energy at 240 meV for the cavity with 50 nm fluorescent film (cavity (b)), figure (4.13b), and there is no coupling upon the cavity with 80 nm florescent film (cavity (c)), figure (4.13c). The exchange energy between the coupled modes is observed in cavities (a) and (b) while it does not exist in the cavity (c). The exchange

energy of coupled system results that the cavity mode and SPP resonance associate their characteristics and thus the coupled system involves two modes with narrow linewidth and strong local field compared with the uncoupled system.

The modal coupling was demonstrated by varying angles from 49 to 52 degree for the three fabricated plasmonic microcavities in figure (4.13). Furthermore, the increase of the thickness of PL film attenuates both cavity and SPP modes. Besides that, the lower mode located in the PL emission linewidth so it exhibits less angle dependency compared to upper mode.

We believe that this is the first and principal report on large Rabi-like splitting for plasmonic microcavity using photoluminescence medium. Beforehand, phase change effect on the PL emission of inserted organic material inside of plasmonic cavity [117] and Rabi-like splitting with J-aggregate thin film on metal layers [118-112] or hybrid metal nanoparticle/J-aggregates systems [111-121] were explored. The single crystal of EY51 (Rubrene-like) adjacent to PMMA polymer can attain high uniformity film deposition by cost-effective solution processing technique and also high carrier mobilities like small organic molecules [122]. These characteristics will overcome many challenges to fabricate high efficiency of organic optoelectronic devices.

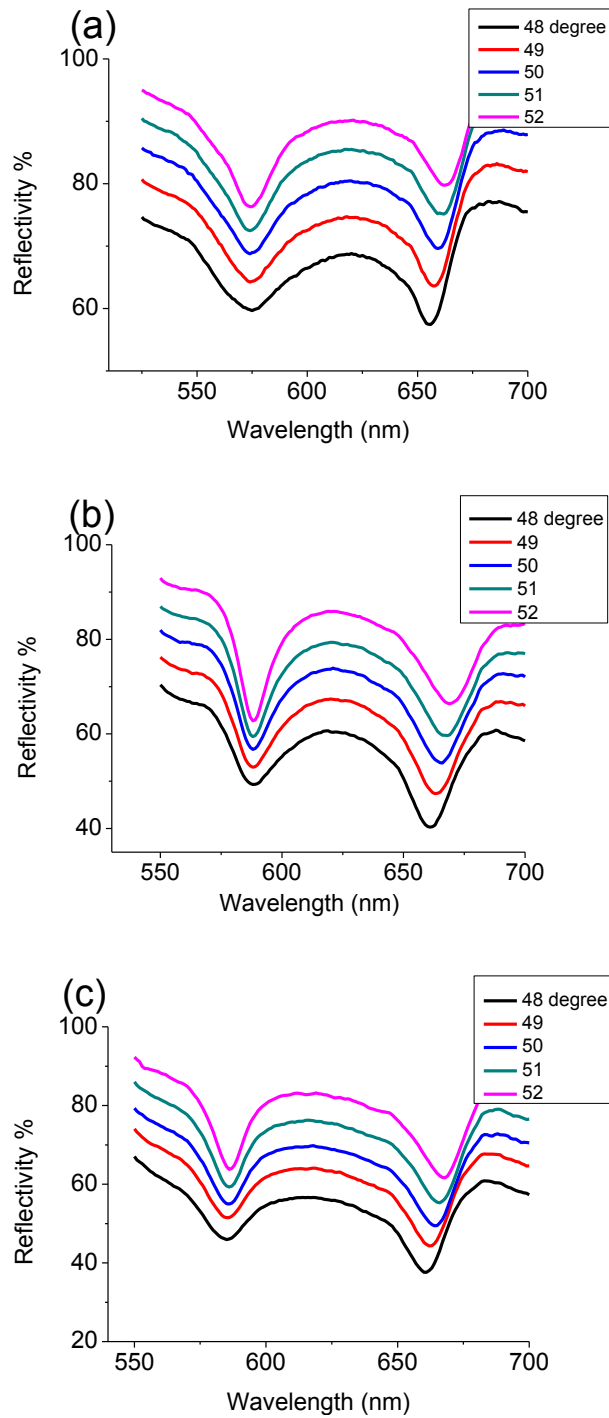


Figure 4.13 . The Rabi-like splitting of strong modal coupling (a) the plasmonic microcavity with 30nm Rubrene layer at 50 degree, (b) the plasmonic microcavity with 50nm Rubrene layer at 50 degree, (c) there is no coupling upon the plasmonic microcavity with 80 nm Rubrene layer.

The PL measurement was performed for plasmonic and photonic microcavity for comparison. The results are shown in figure (4.14a). It is obvious that there is a significant enhancement of PL intensity upon the hybrid plasmonic microcavity which is quite beneficial to decrease the pumping threshold of polariton lasers in the coupled system and serves large improvement of field enhancement inside the cavity. Besides, the photonic microcavity exhibits the cavity mode-exciton coupling with the Rabi splitting around the PL emission peak wavelength 538 nm, the splitting energy equals to 250 meV. The PL emission spectrum of Rubrene coated on PMMA layer was shown in the figure (4.14b).

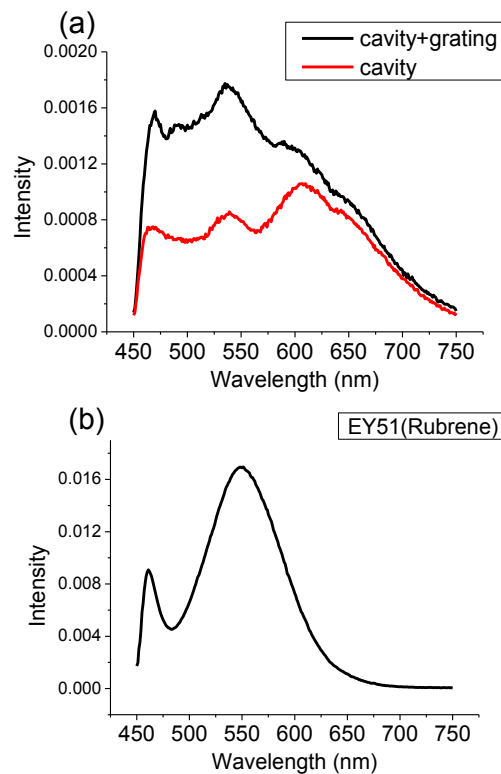


Figure 4.14 The PL emission spectra from (a) the plasmonic and photonic microcavity, (b) Rubrene thin film coated on PMMA layer.

The PL emission involves a weak peak at the wavelength of 470 nm which is related to the emission of PMMA and also the PL emission of Rubrene thin film on PMMA layer shows a blue shift rather than pristine Rubrene on the glass substrate due to the formation of some aggregations on the interface of molecules.

The passive and active plasmonic microcavities demonstrated high quality performance and they can certainly employ in various applications. The plasmonic nanostructure efficiently improved the performance of photonic cavity. In fact, the fabrication technique renders the possibility of making the hybrid plasmonic microcavity on different type of substrates to operate on various ambient conditions.

## **Chapter 5 Conclusion and Future Work**

In this research, the aim is to investigate mode coupling between SPP and microcavity modes using a new hybrid plasmonic device design. The fabrication of plasmonic nanostructure was exploited to make surface plasmon polariton excitation possible at the metal/dielectric interfaces. For this purpose, it was designed two beam laser interference setup for doing photolithography. The photolithography technique is known as a simple practical and economic method to manufacture plasmonic devices, also as a beneficial technique for mass production in industry. The area of fabricated grating can be easily extended to several centimeters by applying expanding/collimating setup of high quality laser beam. The lattice period is generally determined by laser wavelength and the intersecting angle of two-beam interference in laser beam interference. The ruled metal grating was successfully fabricated in large area ( $10 \times 10 \text{ mm}^2$ ) with high uniformity and surface quality. In this work, hybrid plasmonic microcavity was made with two distinct cavity media; passive medium (no absorption) and active medium. The active medium was obtained by adding a thin layer of fluorescent material inside the cavity. The anti-crossing with Rabi-like splitting was observed in both fabricated plasmonic microcavities; in the passive plasmonic microcavity, the splitting energy is 78 meV at the incident angle of 49 degree

whereas the result of the active cavity represents that there is a large splitting energy 280 meV at the incident angle of 50 degree. The absorption effect was investigated on the coupling strength by making cavities with different photoluminescence thick films. It was shown that the coupling strength decreases with enhancement of absorption i.e. the coupling strength is inversely proportional to the absorption coefficient. In addition, the hybrid plasmonic microcavities in large area can be used for commercial requirement application.

Plasmonic nanostructures generate SPP excitations with strong local field but SPP mode suffers from broad linewidth due to high dissipation inside the metal. On the other hand, the cavity mode involves narrow linewidth with the weak local resonance field inside the cavity. The plasmonic microcavity serves to couple cavity mode and SPPs with Rabi-like splitting around common wavelength in the strong coupling regime. Therefore there is exchange energy between two resonance modes where the coupled system possesses two modes with the refined and improved characteristics; strong local field and narrow linewidth. The modified modes can be employed in various applications especially in polariton laser fabrication to decrease pumping threshold and in biosensor to detect small molecules with red shift of SPP excitation wavelength due to refractive index variation. The coupled-uncoupled plasmonic microcavity can also be used as ultrafast optical switch by changing the incident angle or turning on-off the incident light. In this

work, the fabricated plasmonic microcavities indicated satisfying coupling results for promising subsequent applications.

The plasmonic nanostructure can be fabricated with higher dimension such as the square or hexagonal shape aperture of periodic arrays in the next experimental work. The uniformity and area size of plasmonic nanostructures can be improved using high quality laser beam and better expanding/collimating setup besides the lattice constant can be lessened by choosing lower laser wavelength.

The plasmonic nanostructure can be integrated with other optoelectronic devices to optimize the efficiency. It allows arising of light transmission via the coupling of the electromagnetic fields with oscillations of the conductor's electron plasma and satisfying the phase-matching condition at the interface. Subwavelength metal grating serves many devices in several research fields like biosensor, WOLED, harmonic generation, polariton lasers, solar cell, etc.

The large area grating pattern was transferred to the flexible substrate by lift-off technique and resulted in conformal flexible plasmonic structure. This study supports the manufacturing of flexible organic optoelectronic devices in the future.

## References

1. MAIER, STEFAN A. *PLASMONICS:FUNDAMENTALS AND APPLICATIONS*. Springer : s.n., 2007.
2. *Assembly of hybrid photonic architectures from nanophotonic constituents*. Benson, Oliver. s.l. : Nature, 2011, Vol. 480. 193–199.
3. *Light passing through subwavelength apertures*. F. J. Garcia-Vidal, L. Martin-Moreno, T. W. Ebbesen, L. Kuipers. s.l. : REVIEWS OF MODERN PHYSICS., 2010, Vol. 82. 729.
4. *Extraordinary optical transmission through sub-wavelength hole arrays*. T. W. Ebbesen, H. J. Lezec, H. F. Ghaemi, T. Thio, P. A. Wolff. s.l. : NATURE, 1998, Vol. 391.
5. *Room-temperature polariton lasing in an organic single-crystal microcavity*. Forrest, S.K'ena-Cohen and S. R. s.l. : Nat. Photonics, 2010, Vol. 4 . 371 - 375 .
6. Aspects of Nano-Quantum Optics. <https://www.physik.hu-berlin.de/de/nano/lehre/Gastvorlesung%20Wien/NanoQuantum>. [Online]
7. *Microcavity plasmonics: strong coupling of photonic cavities and plasmons*. Giessen, Ralf Ameling and Harald. s.l. : Laser Photonics Rev., 2012. 1-29.
8. *Large-Area Fabrication of Periodic Arrays of Nanoholes in Metal Films and Their Application in Biosensing and Plasmonic-Enhanced Photovoltaics*. Jacson W. Menezes, Jacqueline Ferreira , Marcos J. L. Santos , Lucila Cescato , and Alexandre G. Brolo. s.l. : Adv. Funct. Mater., 2010, Vol. 20. 3918–3924.
9. *Plasma Losses by Fast Electrons in Thin Films*. H, Ritchie R. 1957, Phys. Rev, p. 106 874.
10. *Origin of the Characteristic Electron Energy Losses in Aluminum*. B, Powell C J and Swan J. s.l. : Phys. Rev., 1959, Vol. 115. 869.
11. *Surface Plasma Oscillations of a Degenerate Electron Gas*. A, Stern E A and Ferrell R. s.l. : Phys. Rev, 1960, Vol. 120. 130.

12. *INTERFACES AND THIN FILMS AS SEEN BY BOUND ELECTROMAGNETIC WAVES*. Knoll, Wolfgang. s.l. : Annu. Rev. Phys. Chem., 1998, Vol. 49. 569.
13. Herminghaus S, Vorberg J, Gau H, Conradt R, Reinelt D, Ulmer H, Leiderer P and Przyrembel M. s.l. : Ann.Phys. Lpz., Vol. 6. 425.
14. *Biospecific interaction analysis using biosensor technology*. M, Malmqvist. s.l. : Nature , 1993 , Vol. 261 . 186.
15. M, Braguglia C. s.l. : Chem. Biochem. Eng. Q. , 1998, Vol. 12 . 183.
16. *A sensitivity comparison of optical biosensors based on four different surface plasmon resonance modes*. J, Chien F C and Chen S. s.l. : Biosensors Bioelectron. , 2004 , Vol. 20. 633.
17. *Surface-plasmon microscopy*. BENNO ROTHENHÄUSLER, WOLFGANG KNOLL. s.l. : Nature , 1988, Vol. 332. 615.
18. *Two-Dimensional Imaging of Potential Waves in Electrochemical Systems by Surface Plasmon Microscopy*. Georg Flätgen, Katharina Krischer, Bruno Pettinger, Karl Doblhofer, Heinz Junkes, Gerhard Ertl. s.l. : Science , 1995, Vol. 269. 668.
19. *Surface plasmons as a probe of the electrochemical interface*. J.G. Gordon II, S. Ernst. s.l. : Surf. Sci. , 1980 , Vol. 101 . 499.
20. *Surface plasmon resonance for gas detection and biosensing* . Bo Liedberg, Claes Nylander, Ingemar Lunström. s.l. : Sensors Actuators , 1983, Vol. 4. 299.
21. *Assembly and function of a quaternary signal transduction complex monitored by surface plasmon resonance*. STEPHAN C. SCHUSTER, RONALD V. SWANSON, LISA A. ALEX, ROBERT B. BOURRET and MELVIN I. SIMON. s.l. : Nature, 1993, Vol. 365. 343.
22. *Reliable determination of binding affinity and kinetics using surface plasmon resonance biosensors*. Schuck, Peter. s.l. : Curr. Opin. Biotechnol., 1997 , Vol. 8. 498.
23. *USE OF SURFACE PLASMON RESONANCE TO PROBE THE EQUILIBRIUM AND DYNAMIC ASPECTS OF INTERACTIONS BETWEEN*

- BIOLOGICAL MACROMOLECULES*. Homola J, Yee S S and Gauglitz G. s.l. : Sensors Actuators B , 1999, Vol. 54 . 3.
24. *Protein Interaction Methods-Toward an Endgame*. Andrew R. Mendelsohn, Roger Brent. s.l. : Science, 1999, Vol. 284. 1948.
25. *Surface plasmon resonance analysis of dynamic biological interactions with biomaterials*. Green R J, Frazier R A, Shakesheff K M, Davies M C, Roberts C J and Tendler S J B. s.l. : Biomaterials, 2000, Vol. 21 . 1823.
26. *Extraordinary optical transmission through sub-wavelength hole arrays*. Ebbesen T W, Lezec H J, Ghaemi H F, Thio T and Wolff P A. s.l. : Nature, 1998, Vol. 391. 667.
27. *Beaming Light from a Subwavelength Aperture*. Lezec H J, Degiron A, Devaux E, Linke R A, Martin-Moreno L, Garcia-Vidal F J and Ebbesen T W. s.l. : Science , 2002, Vol. 297. 820.
28. *Hybrid nanoparticle-microcavity-based plasmonic nanosensors with improved detection resolution and extended remote-sensing ability*. Schmidt MA, Lei DY, Wondraczek L, Nazabal V, Maier SA. s.l. : Nat Commun., 2012, Vol. 3. 1108.
29. *Plasmonic Fabry-Pérot nanocavity*. J. Sorger, R. F. Oulton, J. Yao, G. Bartal and X. Zhang. s.l. : Nano Lett., 2009, Vol. 9. 3489.
30. *Plasmonics: Merging Photonics and Electronics at Nanoscale Dimensions*. Ozbay, Ekmel. s.l. : Science, 2006, Vol. 311 . 189.
31. *Nanodot coupler with a surface plasmon polariton condenser for optical far/near-field conversion*. Nomura W, Ohtsu M and Yatsui T. s.l. : Appl. Phys. Lett., 2005, Vol. 86. 181108.
32. *Channel plasmon subwavelength waveguide components including interferometers and ring resonators*. Bozhevilnyi S I, Volkov V S, Devaux E, J.Y. Laluet and Ebbesen T W. s.l. : Nature, 2006, Vol. 440 . 508.
33. *Channel Plasmon-Polariton Guiding by Subwavelength Metal Grooves*. Bozhevilnyi S I, Volkov V S, Devaux E and Ebbesen T W. s.l. : Phys. Rev. Lett., 2005, Vol. 95 . 046802.

34. *Active plasmonics: Controlling signals in Au/Ga waveguide using nanoscale structural transformations*. I, Krasavin A V and Zheludev N. s.l. : Appl. Phys. Lett., 2004, Vol. 84 . 1416.
35. *Active control of surface plasmon–polariton waves*. Krasavin A V, Zayats A V and Zheludev N I. s.l. : J. Opt. A: Pure Appl. Opt., 2005 , Vol. 7 . S85.
36. MAIER, STEFAN A. *PLASMONICS:FUNDAMENTALS AND APPLICATIONS*. s.l. : springer, 2007.
37. H, Kretschmann E and Raether. s.l. : Z. Naturf. A, 1968, Vol. 23. 2135.
38. *Excitation of nonradiative surface plasma waves in silver by the method of frustrated total reflection*. Otto, Andreas. s.l. : Z. Phys. , 1968, Vol. 216 . 398.
39. *Thermal radiative properties of metamaterials and other nanostructured materials: A review*. Ceji FU, Zhuomin M. ZHANG. s.l. : Front. Energ. Power Eng. Chin., 2009 , Vol. 3. 11-26 .
40. *Optical transmission in perforated noble and transition metal films*. F Przybilla, A Degiron, J-Y Laluet, C Genet and T W Ebbesen. s.l. : J. Opt. A, Pure Appl. Opt., 2006, Vol. 8. 458.
41. *Influence of material properties on extraordinary optical transmission through hole arrays*. Sergio G. Rodrigo, F. J. García-Vidal, and L. Martín-Moreno. s.l. : Phys. Rev. B , 2008, Vol. 77. 075401 .
42. *Enhanced transmission of THz radiation through subwavelength holes*. Gomez Rivas, J., C. Schotsch, P. H. Bolivar, and H. Kurz. s.l. : Phys. Rev. B , 2003, Vol. 68. 201306(R).
43. *Resonantly-enhanced transmission through a periodic array of subwavelength apertures in heavily-doped conducting polymer films*. Tatsunosuke Matsui, Z. Valy Vardeny, Amit Agrawal, Ajay Nahata, Reghu Menon. s.l. : Appl. Phys. Lett., 2006, Vol. 88. 071101.
44. *Optical properties of subwavelength hole arrays in vanadium dioxide thin films*. E. U. Donev, J. Y. Suh, F. Villegas, R. Lopez, R. F. Haglund, Jr., and L. C. Feldman. s.l. : Phys. Rev. B , 2006, Vol. 73. 201401.
45. *Modulated optical transmission of subwavelength hole arrays in metal-VO<sub>2</sub> films*. J. Y. Suh, E. U. Donev, R. Lopez, L. C. Feldman and R. F. Haglund Jr. s.l. : Appl. Phys. Lett. , 2006, Vol. 88. 133115 .

46. *Resonant electromagnetic wave transmission through strontium titanate hole arrays with complex surface waves.* Fumiaki Miyamaru, Masaki Tanaka, and Masanori Hangyo. s.l. : Phys. Rev. B, 2006, Vol. 74. 115117.
47. *Midinfrared doping-tunable extraordinary transmission from sub-wavelength gratings.* D Wasserman, EA Shaner, JG Cederberg. s.l. : Appl. Phys. Lett, 2007, Vol. 90. 191102.
48. *Extraordinary optical transmission through subwavelength holes in a polaritonic silicon dioxide film.* Dye-Zone A. Chen, Rafif Hamam, Marin Soljačić, John D. Joannopoulos and Gang Chen. s.l. : Appl. Phys. Lett. , 2007, Vol. 90. 181921.
49. *Optical properties of sub-wavelength hole arrays in SiC membranes.* Y A Urzhumov, D Korobkin, B Neuner , C Zorman and G Shvets. s.l. : J. Opt. A, Pure Appl. Opt., 2007, Vol. 9. S322.
50. *Terahertz Near-Field Imaging Using Enhanced Transmission through a Single Subwavelength Aperture.* Ishihara, K., T. Ikari, H. Minamide, J. Shikata, K. Ohashi, H. Yokoyama, and H. Ito. s.l. : J. Appl. Phys., 2005, Vol. 44. L929.
51. *Effect of hole diameter on terahertz surface-wave excitation in metal-hole arrays.* Fumiaki Miyamaru, Masaki Tanaka, and Masanori Hangyo. s.l. : Phys. Rev. B , 2006, Vol. 74. 153416.
52. *Evidence for radiative damping in surface-plasmon-mediated light transmission through perforated conducting films.* Ahmer Naweed, Frank Baumann, William A. Bailey, Aram S. Karakashian, and William D. Goodhue. s.l. : J. Opt. Soc. Am. B, 2003, Vol. 20. 2534.
53. *Influence of hole size on the extraordinary transmission through subwavelength hole arrays.* van der Molen, K. L., F. B. Segerink, N. F. van Hulst, and L. Kuipers. s.l. : Appl. Phys. Lett. , 2004, Vol. 85. 4316.
54. *Strong influence of hole shape on extraordinary transmission through periodic arrays of subwavelength holes.* Koerkamp KJ, Enoch S, Segerink FB, van Hulst NF, Kuipers L. s.l. : Phys. Rev. Lett., 2004, Vol. 92. 183901.
55. *Polarization control of optical transmission of a periodic array of elliptical nanoholes in a metal film.* Elliott, J., I. I. Smolyaninov, N. I. Zheludev, and A. V. Zayats. s.l. : Opt. Lett. , 2004, Vol. 29. 1414.

56. *Polarization effects in metallic films perforated with a bidimensional array of subwavelength rectangular holes.* Sarrazin, M., and J. P. Vigneron,. s.l. : Opt. Commun., 2004, Vol. 240. 89.
57. *Role of shape and localized resonances in extraordinary transmission through periodic arrays of subwavelength holes: Experiment and theory.* K. L. van der Molen, K. J. Klein Koerkamp, S. Enoch, F. B. Segerink, N. F. van Hulst, and L. Kuipers. s.l. : Phys. Rev. B , 2005, Vol. 72. 045421.
58. *The role of localized surface plasmon modes in the enhanced transmission of periodic subwavelength apertures.* Ebbesen, A. Degiron and T. W. s.l. : J. Opt. A: Pure Appl. Opt. , 2005, Vol. 7. S90–S96.
59. *Surface-plasmon-enhanced transmission through hole arrays in Cr films.* Tineke Thio, H. F. Ghaemi, H. J. Lezec, P. A. Wolff, and T. W. Ebbesen. s.l. : J. Opt. Soc. Am. B, 1999, Vol. 16. 1743.
60. *Finite size effect of transmission property for metal hole arrays in subterahertz.* Hangyo, F. Miyamaru and M. s.l. : Appl. Phys. Lett., 2004, Vol. 84. 2742-2744 .
61. *Multiscale patterning of plasmonic metamaterials.* Henzie, J., M. Lee, and T. Odom. s.l. : Nat. Nanotechnol. , 2007, Vol. 2. 549.
62. *Efficiency and finite size effects in enhanced transmission through subwavelength apertures.* F. Przybilla, A. Degiron, C. Genet, T.W. Ebbesen, F. de Léon-Pérez, J. Bravo-Abad, F. J. García-Vidal, and L. Martín-Moreno. s.l. : Opt. Express, 2008, Vol. 16. 9571.
63. *Microcavity plasmonics: strong coupling of photonic cavities and plasmons.* Giessen, Ralf Ameling and Harald. s.l. : Laser Photonics Rev., 2012. 1-29.
64. Aspects of Nano-Quantum Optics. <https://www.physik.hu-berlin.de/de/nano/lehre/Gastvorlesung%20Wien/NanoQuantum>. [Online]
65. *Weak and strong coupling regimes in plasmonic QED.* T. Hümmer, F. J. García-Vidal, L. Martín-Moreno, and D. Zueco. s.l. : Phys. Rev. B , 2013, Vol. 87. 115419.
66. *Ultrastrongly Coupled Exciton–Polaritons in Metal-Clad Organic Semiconductor Microcavities.* Stéphane Kéna-Cohen, Stefan A. Maier, Donal D. C. Bradley. s.l. : Adv. Optical Mater., 2013, Vol. 1. 827-833.

67. *Strong coupling between surface plasmon polaritons and emitters.* Barnes, P Törmä and W L. s.l. : Rep. Prog. Phys., 2014, Vol. 78.
68. LUKAS NOVOTNY, BERT HECHT. *PRINCIPLES OF NANO-OPTICS.* s.l. : Cambridge University Press, 2006.
69. *Observation of normal-mode splitting for an atom in an optical cavity.* R. J. Thompson, G. Rempe, and H. J. Kimble. s.l. : Phys. Rev. Lett., 1992, Vol. 68. 1132.
70. *Efficient energy exchange between plasmon and cavity modes via Rabi-analogue splitting in a hybrid plasmonic nanocavity.* Shumei Chen, Guixin Li, Dangyuan Lei and Kok Wai Cheah. s.l. : Nanoscale, 2013, Vol. 5. 9129–9133.
71. *An Efficient Large-Area Grating Coupler for Surface Plasmon Polaritons .* Stephan T. Koev, Amit Agrawal, Henri J. Lezec, Vladimir A. Aksyuk. s.l. : Plasmonics, 2012, Vol. 7(2). 269-277 .
72. *Experimental study of the interaction between localized and propagating surface plasmons.* Crozier, Yizhuo Chu and Kenneth B. s.l. : Opt. Letters, 2009, Vol. 34( 3) . 030244 .
73. *Large area plasmonic nanoparticle arrays with well-defined size and shape.* Sarah-Katharina Meisenheimer, Sabrina Jüchter, Oliver Höhn, Hubert Hauser, Christine Wellens, Volker Kübler, Elizabeth von Hauff, Benedikt Bläsi. s.l. : Opt. Mater. EXPRESS 0009, 2014, Vol. 4( 5). 000944.
74. *Recording different geometries of 2D hexagonal photonic crystals by choosing the phase between two-beam interference exposures.* Cescato, J. W. Menezes and L. s.l. : Opt. EXPRESS, 2006, Vol. 14(19). 8578.
75. *Large-area arrays of three-dimensional plasmonic subwavelength-sized structures from azopolymer surface-relief gratings.* Robert J. Moerland, Jenni E. Koskela, Aleksandr Kravchenko, Mikael Simberg, Stefan van der Vegte, Matti Kaivola, Arri Priimagi and Robin H. A. Ras. s.l. : Mater. Horiz., 2014. 1 74-80.
76. *Plasmonic Nanopillar Arrays for Large-Area, High-Enhancement Surface-Enhanced Raman Scattering Sensors.* Joshua D. Caldwell, Orest Glembocki, Francisco J. Bezares, Nabil D. Bassim, Ronald W. Rendell, Mariya Feygelson, Maraizu Ukaegbu, Richard Kasica, Loretta Shirey, and Charles Hosten. s.l. : Acs. Nn. , 2011, Vol. 5(5). 4046–4055.

77. *review of roll-to-roll nanoimprint lithography*. A Nazrin Kooy, Khairudin Mohamed, Lee Tze Pin and Ooi Su Guan. s.l. : Nanoscale Res. Lett. , 2014, Vol. 9 . 320 .
78. *Large-Area Fabrication of Periodic Arrays of Nanoholes in Metal Films and Their Application in Biosensing and Plasmonic-Enhanced Photovoltaics*. Jacson W. Menezes, Jacqueline Ferreira , Marcos J. L. Santos , Lucila Cescato and Alexandre G. Brolo. 2010 : Adv. Funct. Mater., Vol. 20. 3918–3924.
79. Helbert, William B. Glendinning and John N. *Handbook of VLSI Microlithography; Principles, Technology and Applications*. s.l. : NOYES PUBLICATIONS, 1991.
80. Stefan Sinzinger, Jurgan Jahns. *Microoptics* . s.l. : WILEY-VCH, 1999.
81. Brenner, Jurgan Jahns and Karl-Heinz. *Microoptics From Technology to Applications*. s.l. : Springer, 2004.
82. Hecht, Eugene. *Optics, 4th ed.* s.l. : Addison Wesley, 2002.
83. Positive Photoresists for lift-off-application AR-P 5300. [Online] 2013. <http://www.allresist.com/>.
84. Stefan Sinzinger, and Jurgan Jahns. *Microoptics*. s.l. : WILEY-VCH, 1999.
85. Parameter collection AR-Resists. [Online] 2013. <http://www.allresist.com/>.
86. Vijitha, Viji. *Ellipsometry- non destructive measuring method*. [Online] 2014. <http://www.slideshare.net/foolishcrack/ellipsometry>.
87. Irene, Harland G. Tompkins and Eugene A. *HANDBOOK OF ELLIPSOMETRY*. s.l. : Springer, 2005.
88. MAIER, STEFAN A. *PLASMONICS:FUNDAMENTALS AND APPLICATIONS*. s.l. : Springer, 2007.
89. *Room-temperature polariton lasing in an organic single-crystal microcavity*. Forrest, S.K'ena-Cohen and S. R. s.l. : Nat. Photonics , 2010, Nat. Photonics 4, Vol. 4, pp. 371 - 375 . 371 - 375 .
90. *Nanostructured Plasmonic Sensors*. Matthew E. Stewart, Christopher R. Anderton, Lucas B. Thompson, Joana Maria, Stephen K. Gray, John A. Rogers, and Ralph G. Nuzzo. s.l. : Chem. Rev. , 2008, Vol. 108. 494-521.

91. *Plasmonic gold mushroom arrays with refractive index sensing figures of merit approaching the theoretical limit.* Yang Shen, Jianhua Zhou, Tianran Liu, Yuting Tao, Ruibin Jiang, Mingxuan Liu, Guohui Xiao, Jinhao Zhu, Zhang-Kai Zhou, Xuehua Wang, Chongjun Jin, Jianfang Wang. s.l. : 2013, ncomms., Vol. 4. 3381.
92. *Extremely sub-wavelength THz metal-dielectric wire microcavities.* Chery Feuillet-Palma, Yanko Todorov, Robert Steed, Angela Vasanelli, Giorgio Biasio, Lucia Sorba, and Carlo Sirtori. s.l. : Opt. EXPRESS, 2012, Vol. 20(27). 29121.
93. *Microcavity plasmonics: strong coupling of photonic cavities and plasmons.* Giessen, Ralf Ameling and Harald. s.l. : Laser Photonics Rev., 2012. 1–29.
94. *Large-Area Fabrication of Periodic Arrays of Nanoholes in Metal Films and Their Application in Biosensing and Plasmonic-Enhanced Photovoltaics.* Jacson W. Menezes, Jacqueline Ferreira, Marcos J. L. Santos, Lucila Cescato and Alexandre G. Brolo. s.l. : Adv. Funct. Mater., 2010, Vol. 20. 3918–3924.
95. Corp., MicroChem. [microchem.com/pdf/PMMA\\_Data\\_Sheet.pdf](http://microchem.com/pdf/PMMA_Data_Sheet.pdf). [Online] 2001. WWW.MICROCHEM.COM.
96. *Microcavity plasmonics: strong coupling of photonic cavities and plasmons.* Giessen, Ralf Ameling and Harald. s.l. : Laser Photonics Rev., 2012, Laser Photonics Rev., pp. 1–29.
97. *Strong coupling between surface plasmon polaritons and emitters.* Barnes, P. Törma and W. L. 2015, Rep. Prog. Phys., Vol. 78.
98. Lukas Novotny, Bert Hecht. *PRINCIPLES OF NANO-OPTICS*. s.l. : Cambridge University Press, 2006.
99. *Cavity Plasmonics: Large Normal Mode Splitting of Electric and Magnetic Particle Plasmons Induced by a Photonic Microcavity.* Giessen, Ralf Ameling and Harald. 2010, Nano Lett., Vol. 10, pp. 4394–4398.
100. *Coupling of plasmonic and optical cavity modes in quasi-three-dimensional plasmonic crystals.* Debashis Chanda, Kazuki Shigeta, Tu Truong, Eric Lui, Agustin Mihi, Matthew Schulmerich, Paul V. Braun, Rohit Bhargava, and John A. Rogers. 2011, Nat. Commun., Vol. 2, p. 479.

101. *Plasmonic Fabry-Pe´rot Nanocavity*. Volker J. Sorger, Rupert F. Oulton, Jie Yao, Guy Bartal, and Xiang Zhang. 2009, Nano Lett., Vol. 9, p. 10.
102. *Ultrastrongly Coupled Exciton-Polaritons in Metal-Clad Organic Semiconductor Microcavities*. Stéphane Kéna-Cohen, Stefan A. Maier and Donald D. C. Bradley. 2013, Adv. Optical Mater., Vol. 1, pp. 827-833.
103. *Efficient energy exchange between plasmon and cavity modes via Rabi-analogue splitting in a hybrid plasmonic nanocavity*. Shumei Chen, Guixin Li, Danyuan Lei and Kok Wai Cheah. 2013, Nanoscale, Vol. 5, pp. 9129–9133.
104. *Strong coupling in hybrid plasmon-modulated nanostructured cavities*. Zhen-Yu Zhang, Hai-Yu Wang, Jiang-Lin Du, Xu-Lin Zhang, Ya-Wei Hao, Qi-Dai Chen and Hong-Bo sun. 2014, Applied Phys. Lett., Vol. 105 (19), p. 191117.
105. *Coupling Enhancement and Giant Rabi-Splitting in Large Arrays of Tunable Plexcitonic Substrates*. Panit Chantharasupawang, Laurence Tetard and Jayan Thomas. 2014, Phs. Chem. C , Vol. 108, pp. 23954-23962.
106. *Strong exciton- photon Coupling in an organic semiconductor microcavity*. D. G. Lidzey, D. D. C. Bradley, M. S. Skolnick, T. Virgili, S. Walker, and D. M. Whittaker. 1998, Nature, Vol. 395(6697), pp. 53–55.
107. *Strong exciton-photon coupling in organic materials*. Forrest, R. J. Holmes and S. R. 2007, Org. Electron., Vols. 8(2-3), pp. 77–93.
108. *Role of intramolecular dynamics on intermolecular coupling in cyanine dye*. T. Virgili, L. Lüer, G. Cerullo, G. Lanzani, S. Stagira, D. Coles, A. J. H. M. Meijer, and D. G. Lidzey. 2010, Phys. Rev. B, Vol. 81(12), p. 125317.
109. *Strong exciton-photon coupling and exciton hybridization in a thermally evaporated polycrystalline film of an organic small molecule*. Forrest, R.J. Holmes and S.R. 2004, Phys. Rev. Lett., Vol. 93 (18) , p. 186404.
110. *Ultrafast Manipulation of Strong Coupling in Metal-Molecular Aggregate Hybrid Nanostructures*. P. Vasa, R. Pomraenke, G. Crimi, E. De Re, W. Wang, S. Schwieger, D. Leipold, E. Runge, G. Cerullo and C. Lienau. 2010, ACS Nano, Vol. 4 (12), pp. 7559-7565.
111. *Rabi Splitting in Photoluminescence Spectra of Hybrid Systems of Gold Nanorods and J-Aggregates*. Dzmitry Melnikau, Ruben Esteban, Diana Savateeva, Ana Sánchez-Iglesias, Mark Grzelczak, Mikolaj K. Schmidt, Luis

M. Liz-Marzán, Javier Aizpurua and Yury P. Rakovich. 2016, Phys. Chem. Lett., Vol. 7, pp. 354-362.

112. *Adjustable exciton-photon coupling with giant Rabi-splitting using layer-by-layer J-aggregate thin films in all-metal mirror microcavities.* Huang-Sen Wei, Cheng-Chung Jaing, Yan-Ting Chen, Chen-Chih Lin, Ching-Wei Cheng, Chia-Hua Chan, Cheng-Chung Lee and Jui-Fen Chang. 2013, Opt. EXPRESS, Vol. 21 (18), pp. 21365-21373.

113. *Exciton Plasmon Coupling Enhancement via Metal Oxidation.* Francesco Todisco, Stefania D'Agostino, Marco Esposito, Antonio I. Fernández-Domínguez, Milena De Giorgi, Dario Ballarini, Lorenzo Dominici, Iolena Tarantini, Massimo Cuscuna', Fabio Della Sala, Giuseppe Gigli, and Daniele Sanvitto. 2015, ACS Nano, Vol. 9 10, pp. 9691–9699.

114. *Large-Area Fabrication of Periodic Arrays of Nanoholes in Metal Films and Their Application in Biosensing and Plasmonic-Enhanced Photovoltaics.* Jacson W. Menezes, Jacqueline Ferreira, Marcos J. L. Santos, Lucila Cescato and Alexandre G. Brolo. 2010, Adv. Funct. Mater., Vol. 20, pp. 3918–3924.

115. *Surface-enhanced second-harmonic diffraction: Experimental investigation of selective enhancement.* Andrew C. R. Pipino, Richard P. Van Duyne, and George C. Schatz. 1996, Physical Rev. B, Vol. 53 7, p. 4162.

116. *Organic field-effect transistors using crystals.* Takeya, Tatsuo Hasegawa and Jun. 2009, Sci. Technol. Adv. Mater., Vol. 10, p. 024314.

117. *Plasmonic microcavity using photo-reduced silver nanoparticles and light-emitting polymer.* Feifei Liu, Xiping Zhang, Xiaohui Fang and Yuanhai Lin. 2016, Opt. EXPRESS, Vol. 24 (2), pp. 1747-1757.

118. *Vacuum Rabi Splitting and Strong-Coupling Dynamics for Surface-Plasmon Polaritons and Rhodamine 6G Molecules.* T. K. Hakala, J. J. Toppari, A. Kuzyk, M. Pettersson. H. Tikkanen, H. Kunttu and P. Törmä. 2009, Phys. Rev. Lett., Vol. 103 (5), p. 053602(4).

119. *Plasmonic Surface Lattice Resonances at the Strong Coupling Regime.* A. I. Väkeväinen, R. J. Moerland, H. T. Rekola, A.P. Eskelinen, J.P. Martikainen, D.H. Kim, and P. Törmä. 2014, Nano Lett., Vol. 14, p. 1721–1727.

120. *Approaching the strong coupling limit in single plasmonic nanorods interacting with J-aggregates.* Gu'lis Zengin, Go'ran Johansson, Peter Johansson, Tomasz J. Antosiewicz, Mikael Ka'll and Timur Shegai. 2013, *Scientific Reports*, Vol. 3, p. 3074.

121. *Molecular Plasmonics with Tunable Exciton-Plasmon Coupling Strength in J-Aggregate Hybridized Au Nanorod Assemblies.* Gregory A. Wurtz, Paul R. Evans, William Hendren, Ronald Atkinson, Wayne Dickson, Robert J. Pollard, and Anatoly V. Zayats. 2007, *Nano Lett.*, Vol. 7 5, pp. 1297-1303.

122. P. S. Jo, D. T. Duong, J. Park, R. Sinclair, A. Salleo. 2015, *Chem. Mater.*, Vol. 27, pp. 3979-3987.

## **Curriculum Vitae**

Academic Qualifications of the thesis author, Mrs. Fatemeh Hosseini Alast:

- Received the degree of Bachelor of Science in Physics (Major in Solid States) from International University of Imam Khomeini (Iran), June 2005.
- Received the degree of Master of Science in Photonics (Fabrication of Microlens Array by Thermal Reflow Method and Replication with Soft Molding Process) from Shahid Beheshti University (Iran), August 2008.

April 2017